variation. However, VET (=153.2±18.9 msec) was found to be inversely correlated with heart rate as reported by other studies on VET [7].

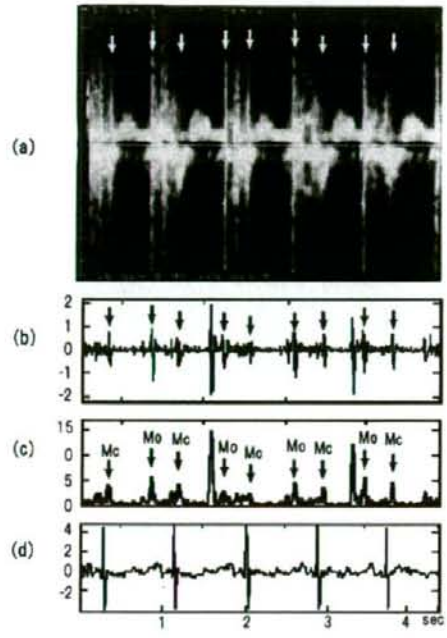

Figure 4. Upper panel (a) shows the example of Pulsed-wave Doppler signals of fetal mitral valve movements annotated to show how the specific signals are linked with opening and closing events. Mo and Mc represent the opening and closing of mitral valve. The lower panels show Doppler signals and its wavelet decomposition at level 2. Panel (b) shows the Doppler signals from fetal monitor 116. (c) shows the wavelet decomposition of Doppler signals at level 2. (d) shows the simultaneous fetal electrocardiogram signals.

Table 1: Summary of time intervals of opening and closing of the aortic and mitral valves from FECG over each cardiac cycle. Mean R-R intervals [403.6±17.8 msec (N=680)].

	Q-Mc	Q-Ao	Q-Ac	Q-Mo
Mean (msec)	45.0	75.0	221.6	301.6
SD	18.9	11.9	29.0	20.7

4. Conclusions

Fetal ECG and Doppler ultrasound signals provide clinically significant information concerning the physiological state of a fetus. Multiresolution wavelet analysis enabled the frequency contents of the Doppler signals to be linked to the opening and closing of the aortic and mitral valves as confirmed by M-mode and pulsed Doppler. These results suggest means by which the cardiac events that contribute to the Doppler signal may be distinguished, providing information for better recognizing the fetal arrhythmia, anoxia and heart failure.

Acknowledgements

This study was supported by an Early career researcher (ECR) grant awarded to AH Khandoker by University of Melbourne. Additionally, partial supports were received from Australian Research Council (ARC) Intelligent sensing, sensor networks and information processing (ISSNIP) research network.

References

[1] Ferencz C, Rubin JD, McCarter RJ. Congenital heart disease: prevalence at live birth. The Baltimore-Washington infant study. Am J Epidemiol 1985;121: 31–6

[2] Bonnet D, Coltri A, Butera G, et al. Detection of transposition of the great arteries in fetuses reduces neonatal morbidity and mortality. Circulation 1999; 99:916–8

[3] Schwartz PJ. The long QT syndrome. Curr Probl Cardiol 1997;22: 297–351.

[4] Vigliani M. Romano–Ward syndrome diagnosed as moderate fetal bradycardia: a case report. J Reprod Med. 1995; 40: 725–728

[5] Hofbeck M, Ulmer H, Beinder E, Sieber E, Singer H. Prenatal findings in patients with prolonged QT interval in the neonatal period. Heart.1997; 77: 198–204.

[6] Matonia A, Jezewski J, Kupka T, Wrobel J, Horoba K, Widera M. Instrumentation for Fetal Cardiac Performance Analysis During the Antepartum Period. Proceedings of the IEEE Engineering in Medicine and Biology 27th Annual Conference, NY,2005; 1-4.

[7] Murata Y and Martin, C. B. Systolic time intervals of the fetal cardiac cycle, Obstet. Gynecol.,1974; 44: 224-232

[8] Sato M, Kimura Y, Chida S., Ito T, Katayama N, Okamura K., Nakao M. A Novel Extraction Method of Fetal Electrocardiogram From the Composite Abdominal Signal. IEEE Trans on Biomed Engg., 2007; 54 (1): 49-58.

[9] Goodlin R.C., Girard J., Hollmen A. "Systolic time intervals in the fetus and neonate", Circulation, 1968; 37: 149-159.

Address for correspondence
Ahsan Khandoker
Dept. of Electrical & Electronic Engg. The University of Melbourne, VIC -3010, Australia.
E-mail: a.khandoker@ee.unimelb.edu.edu.au

30th Annual International IEEE EMBS Conference
Vancouver, British Columbia, Canada, August 20-24, 2008

Robustness of the Blind Source Separation with Reference against Uncertainties of the Reference Signals

Tomoyuki Netabayashi, Yoshitaka Kimura, Shinichi Chida, Takuro Ito, Kazunari Ohwada, Norihiro Katayama, Kunihiro Okamura, and Mitsuyuki Nakao, *Member, IEEE*

Abstract—**The fetal electrocardiogram (ECG) could provide clinical information concerning physiological conditions of the fetus. In order to extract fetal ECG, we proposed the novel algorithm, the blind source separation with reference (BSSR), which successfully extracts a complete waveform of QRS complex and avoids uncertainty in the order of the extracted signals. In the BSSR, the reference signal is supposed to be generated from the ultrasonic Doppler signal. Thus generated reference is expected to suffer from uncertainties in waveform and occurrence timing. Based on simulations, the BSSR is shown to have robustness against the uncertainties of reference signals. In addition, it is shown how the robustness depends on the order of power of correlation function between the reference and extracted signals, which composes a performance function of the BSSR.**

I. Introduction

A FETAL electrocardiogram (ECG) provides clinically significant information concerning physiological states of a fetus. For example, arrhythmias show the immaturity of fetal cardiac activity, and anoxia is known to alter the balance between the electrical polarization and repolarization of heart [1]. Ultrasonic measurements of physical motions of the heart could not provide the electrophysiological information. Nevertheless, the fetal ECG has not yet been popularly used in the clinical situations, because there is no low cost and reliable method to measure the fetal ECG. The magnetocardiogram (MCG) could directly monitor the electrical activity of fetal heart, which is measured by placing a SQUID probe close to the fetus over the mother's abdomen [2]. However, the MCG measurement needs a special large scale equipment [2]. Instead, the signal processing methods extracting the fetal ECG signal from the composite abdominal signal have been developed [3],[4]. Especially, the independent component analysis (ICA) or blind source separation (BSS) have been applied to this problem [5],[6]. In comparison with them, our proposed algorithm, BSSR (blind source separation with reference), realizes better performances in the following points [7]. The BSSR successfully extracts a complete waveform of QRS complex and avoids uncertainty in the order of the extracted signals. This algorithm is characterized by usage of the reference signal which mimics a source signal to be restored. For extracting ECG, the reference is a sequence of spike-like events each of which corresponds to a heart beat. Actually, the reference signal is supposed to be generated from the ultrasonic Doppler signal which is usually monitored in clinical diagnosis. According to our preliminary study, a generated reference signal from the Doppler signal is thought to suffer from uncertainties in waveform and occurrence timing, because the Doppler signals have inherently random nature in shape [8]. It is not clarified how these uncertainties affect performance of the BSSR.

In this paper, how performance of the BSSR depends on the uncertainties of the reference signals are clarified by simulations. In addition, it is investigated how this dependency is modified by the order of power of correlation function between the reference and extracted signals, which composes a performance function of the BSSR [7]. Through these simulation studies, permissible range of uncertainties of the reference is clarified for the BSSR. This result could provide necessary conditions for us to develop a generation method of the reference from the ultrasonic Doppler signal.

Manuscript received April 7, 2008. This work was supported in part by Special Coordination Funds for Promoting Science and Technology and by the "Academic Frontiers" Project for Private Universities (Kansei Fukushi Research Center of Tohoku Fukushi University) through a matching fund subsidy from the Ministry of Education, Culture, Sports, Science and Technology of Japan.

T.Netabayashi, N.Katayama, and M.Nakao are with Graduate School of Information Sciences, Tohoku University, Sendai 980-8579, Japan (corresponding author to provide phone & fax: +81-22-795-7157; e-mail: nakao@ecei.tohoku.ac.jp).

Y.Kimura and T.Ito are with TUBERO, Tohoku University, Sendai 980-8575, Japan

S.Chida is with TESCO Co. Ltd., Sendai 980-0832, Japan

K.Ohwada is with Atom Medical Co. Ltd., Tokyo 113-0033, Japan

K.Okamura is with Graduate School of Medicine, Tohoku University, Sendai 980-8575, Japan

II. Algorithm of Blind Source Separation with Reference and Simulation Conditions

A. Algorithm of BSSR

The data are pre-whitened, i.e., the covariance matrix of the data is diagonalized [8]. The method is formulated as follows. Let us consider a situation that n source signals $\mathbf{s}=(s_1, s_2, \cdots, s_n)$ are observed as $\mathbf{x}=(x_1, x_2, \cdots, x_m)$ through a linear and immediate mixture $\mathbf{x}=A\mathbf{s}$, where A denotes the full rank mixing matrix of $m \times n$. Our purpose is to estimate A and $\mathbf{s}$. Here, the estimation of individual source signal is considered separately, $y=\mathbf{w}^T\mathbf{x}$, where y and $\mathbf{w}$ denote estimates of a source signal and the corresponding row vector of the estimated inverse of A, respectively. T denotes a transpose. Here, note that only a few sources are needed to be recovered out of m observations. They are fetal ECGs which consist of almost periodic sequence of pulse-like events. In this sense,

978-1-4244-1815-2/08/$25.00 ©2008 IEEE.

the situation is not a completely blind one. In order to aid the estimation, an artificial or observable signal closely related to the source signal to be recovered is referred to. Now, we think of estimating y which is highly correlated with the reference signal r under the constraint $|\mathbf{w}|=1$. This is realized by maximizing the Lagrangian:

$$L(\mathbf{w}) = \frac{1}{2k} E[y^{2k} r^{2k}] - \frac{\lambda}{2}(\mathbf{w}^T\mathbf{w} - 1), \qquad (1)$$

where $E[\ ]$ denotes an expectation, and λ is a Lagrange multiplier [7]. Here, the correlation $E[y^{2k} r^{2k}]$ is called "performance function" [9]. As a solution of (1), we have

$$\mathbf{w} = \frac{E[y^{2k-1} r^{2k} \mathbf{x}]}{E[y^{2k} r^{2k}]} . \qquad (2)$$

Actually, the following interations give the solutions.

$$\mathbf{w}_{n+1} = \frac{E[y_n^{2k-1} r^{2k} \mathbf{x}]}{E[y_n^{2k} r^{2k}]} \qquad (3)$$

$$y_{n+1} = \mathbf{w}_{n+1}^T \mathbf{x} .$$

The practical estimation is performed as follows. The initial value of $\mathbf{w}$ is given as a vector whose entries take ± 1 at random. This is only for starting algorithm with not so strong preference. The extraction is done in a segment-wise manner, where one segment is 5s (5,000 points). The expectation is realized by the temporal integration in the respective segment. k=2 unless otherwise stated. The details of our algorithm were explained in comparison with previously proposed methods elsewhere [7].

B. *Simulation Conditions*

For simulations, we use test source signals shown in Fig.1. Among them, ch.1-ch.3 are separated a priori from the actual composite abdominal signal. Note that 4th power of Gaussian noise resembles ECG in its statistical properties. The observed signal subject to separation is obtained through

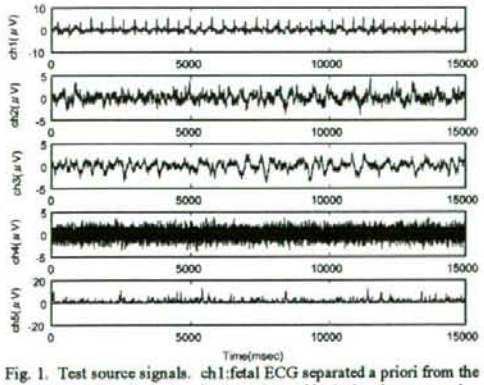

Fig. 1. Test source signals. ch1:fetal ECG separated a priori from the composite abdominal signal, ch2, ch3:residual signals separated a priori from the composite abdominal signal, ch4:Gaussian noise, ch5: 4th power of Gaussian noise.

operating an appropriate 5×5 mixing matrix ([0.203 0.0153 0.419 0.838 5.03; 0.199 0.747 0.846 0.0196 7.09; 0.604 0.445 0.525 0.681 4.29; 0.272 0.932 0.203 0.380 3.05; 0.199 0.466 0.672 0.832 1.90]) on the test source signal.

The reference signal is a sequence of spike-like event shaped by $\cos 2\pi(t-t_p)/d$, $|t-t_p| \le d/2$, where t denotes the time, t_p indicates the peak position of the reference event, and d denotes width of event. In order to include basic uncertainty, a timing of each event is randomly shifted following a uniform distribution around occurrence of R

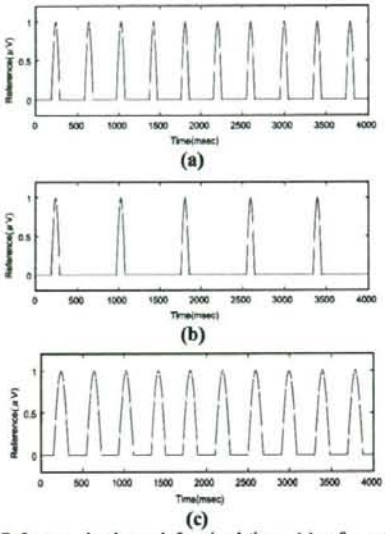

Fig.2. Reference signals used for simulations. (a) reference signal (d=100ms). (b) reference signal decimated by a rate of 0.5 (d=100ms). (c) reference signal consists of width-varied events (d=180ms)

wave of the fetal ECG in ch.1. Thus constructed reference signal is shown in Fig.2(**a**). Furthermore, we add other types of uncertainty to this reference signal: decimation of reference events by a rate of 0.5 or 0.125 (Fig.2(**b**) for 0.5), and variation of event width 20ms or 180ms (Fig.2(**c**) for d=180ms).

III. Simulation Results

A. *Fundamental Performance of BSSR*

Fig.3(**a**) shows the fundamental performance of the BSSR against uncertainty in timing of reference event, where a correlation of the extracted signal with the ECG signal (source 1) is plotted as a function of the range of uniform distribution for random shifting. Simulations ran 50 times with different sample processes of noise signals (sources 4 and 5), and averaged results are shown. This plot indicates how the ECG signal is contained in each extracted channel. Naturally, it is desirable that a single channel exclusively contains the ECG signal. In this figure, the correlation in ch.1 is gradually degraded beyond the shift range of 40ms, and instead those in the other channels increase, i.e., the ECG signal becomes scattered over the channels. This result

indicates that full recovery of the ECG signal becomes difficult as the timing of reference event more largely deviates from the correct position. This could be understood from deterioration of the performance function as shown in Fig.3(b). That is, the performance function for the ECG signal monotonically decreases associated with an extension of shift range. In contrast, the 4^{th} power of Gaussian noise (source 5) raises its performance function. This is due to highly randomized reference signal resembles the 4^{th} power of Gaussian noise in a statistical sense. It is worth noting that the degradation of performance of ECG extraction coincides with an increase of the performance function for the source 5.

B. Performance of BSSR with decimated reference signals

Fig.4 shows how the 1/2 decimation of reference event affects the performance of the BSSR. In Fig.4(a), the correlation for ECG signal in ch.1 is shown to be retained until the shift range of 70ms, but to deteriorate little bit more rapidly than the case of no decimation. This could be understood from behavior of the performance function shown in Fig.4(b). Although the absolute value itself is almost halved, the performance function decreases with a similar rate to the case of no decimation. A distinct thing is that the build-up of performance function for the source 5 begins around the shift range of 70ms or larger, which coincides again with the collapse of correlation in ch.1. In the case of 1/8 decimation, value of the performance function for the ECG signal was an eighth of the case with a complete reference signal, and the build-up of the performance function for the source 5 began around the shift range of 120ms (the results were omitted). Although the correlation in ch.1 was always lower than 1, it decreased more gradually than the case with a complete reference as well as 1/2 decimation.

C. Performance of BSSR with varied width of reference event

Fig.5 shows the performance of the BSSR with the width of reference event d=180ms. Characteristically, the correlation in ch.1 is shown to be maintained close to 1 up to the shift range of 70ms, and to decrease rapidly beyond this critical range of shift. In addition, the correlations in ch.2 and ch.3 are built-up more rapidly in comparison with the

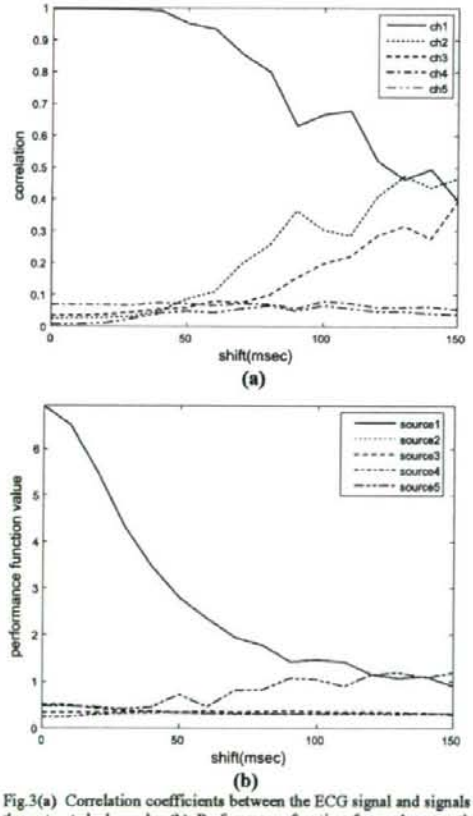

Fig.3(a) Correlation coefficients between the ECG signal and signals in the extracted channels. (b) Performance function for each extraction. Shift value indicates a deviation range from the center of the uniform distribution. d=100ms..

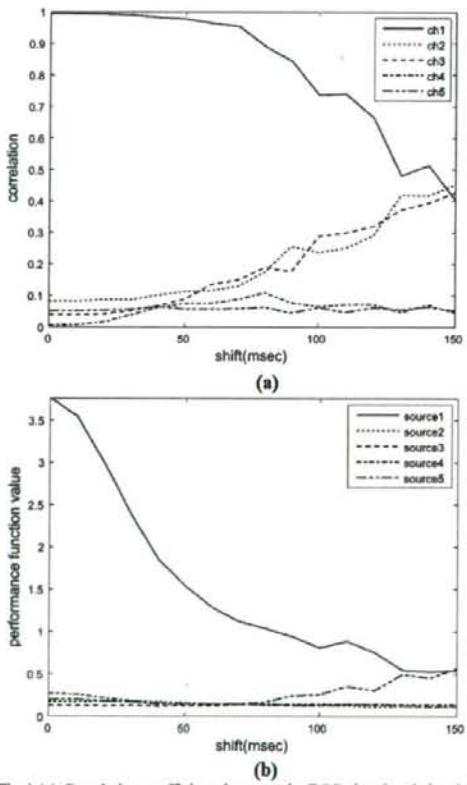

Fig.4 (a) Correlation coefficients between the ECG signal and signals in the extracted channels with 1/2 decimated reference signal. (b) Performance function for each extraction. Shift value indicates a deviation range from the center of the uniform distribution. d=100ms..

case of d=100ms. This wider range of shift allowing acceptable performance of the BSSR could be understood from the behavior of performance function. The performance function for the ECG signal more gradually decreases and that for the 4th power of Gaussian noise more rapidly increases in comparison with the case of d=100ms. In contrast, under the condition of d=20ms the correlations in ch.1 and in chs.2 and 3 were progressively reduced and built-up from a further smaller range of shift than d=100ms, respectively (the results were omitted here). As easily expected, the performance function for the ECG signal more steeply decreased under d=20ms than d=100ms.

D. Robustness of BSSR dependent on the order of performance function

In the previous simulations, the robustness of the BSSR against various kinds of uncertainties in the reference signal was investigated, which showed that the performance of the BSSR could be well understood based on the performance function. Naturally, the robustness of the BSSR is expected to depend on the order of the performance function which is denoted by $2k$. This dependency was examined by simulations. Here, the results are only summarized. As for k=1, although the performance function for the ECG signal dominated the others, the performance function for the Gaussian noise was relatively large, which could be responsible for the extraction performance that the ECG signal leaked into a few channels. As for k=4, the ECG signal significantly leaked into another channel in addition to ch.1 even under small range of shift over 30ms. This is possibly due to the fact that the performance function for the 4th power of Gaussian noise was rapidly built-up and exceeded that for the ECG signal over the shift of 30ms. In other words, it is difficult for the eighth power of correlation $E[y^8 r^8]$ to distinguish between the ECG signal and the 4th power of Gaussian noise.

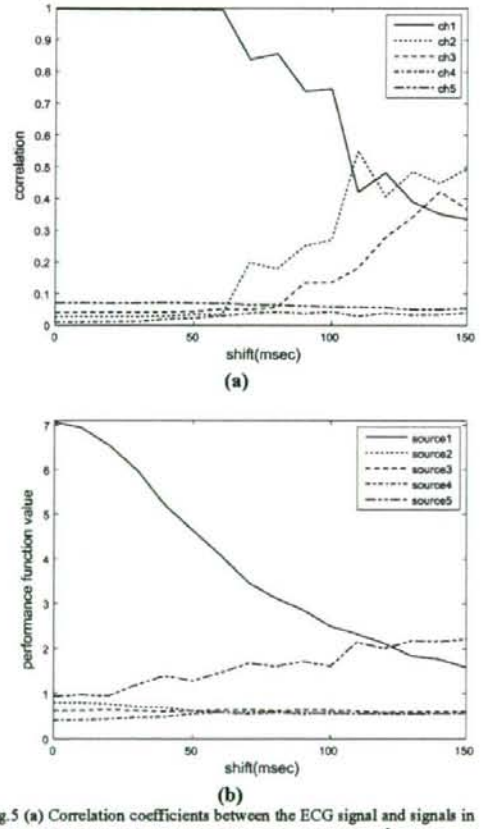

Fig.5 (a) Correlation coefficients between the ECG signal and signals in the extracted channels with the reference event width d=180ms. (b) Performance function for each extraction. Shift value indicates a deviation range from the center of the uniform distribution.

IV. Conclusion

Through the simulations, the BSSR was shown to have robustness against various kinds of uncertainties in the reference signal. The performance of the BSSR could be well understood in terms of the behavior of performance function. These results provide useful information concerning permissible uncertainties of the reference signal. In addition, because the performance of the BSSR depends on the order of the performance function, it could be a possible strategy that the order of the performance function is selected responsible for what kinds of noise are expected to be contained in observed signals. Generalization of our findings will be a future subject.

References

[1] E.M. Symonds, D. Sahota, and A. Chang, *Fetal Electrocardiology*. London: Imperial College Press, 2001.

[2] *Fetal Cardiogram Database*, Aug. 2004 [Online]. Available: http://bct.tn.utwente.nl

[3] A. Khamene and S. Negahdaripour, "A new method for the extraction of fetal ECG from the composite abdominal signal," *IEEE Trans. Biomed. Eng.*, vol.47, pp.507-516, April 2000.

[4] V. Zarzoso and A.K.Nandi, "Noninvasive fetal electrocardiogram extraction: Blind separation versus adaptive noise cancellation," *IEEE Trans. Biomed. Eng.*, vol.48, pp.12-18, Jan 2001.

[5] L. De Lathauwer, B. De Moor, and J. Vandewalle, "Fetal electrocardiogram extraction by blind source subspace separation," *IEEE Trans. Biomed. Eng.*, vol.47, pp.567-572, May 2000.

[6] M.J.O. Tayler, M.J. Smith, M. Thomas, A.R. Green, F. Cheng, S. Oseku-Afful, L.Y. Wee, N.M. Fisk, and H.M. Gardiner, "Non-invasive fetal electrocardiography in singleton and multiple pregnancies," *Int. J. Obstet. Gynaecol.*, vol.110, pp.668-678, July 2003.

[7] M.Sato, Y.Kimura, S.Chida, T.Ito, N.Katayama, K.Okamura, and M.Nakao, "A novel extraction method of fetal electrocardiogram from the composite abdominal signal," *IEEE Trans. Biomed. Eng.*, vol.54, pp.49-58, 2007.

[8] T. Netabayashi, "A method for extracting fetal ECG based on the BSSR," Master Thesis, GSIS, Tohoku Univ, 2008.

[9] A. Cichocki and S. Amari, *Adaptive Blind Signal and Image Processing*, West Sussex, U.K.: Wiley, 2002.

THE JOURNAL OF BIOLOGICAL CHEMISTRY VOL. 284, NO. 9, pp. 5685–5696, February 27, 2009

Molecular Determinants Differentiating Photocurrent Properties of Two Channelrhodopsins from *Chlamydomonas*[*] [S]

Received for publication, October 2, 2008, and in revised form, December 17, 2008 Published, JBC Papers in Press, December 22, 2008, DOI 10.1074/jbc.M807632200

Hongxia Wang[‡§], Yuka Sugiyama[§¶], Takuya Hikima[‡§], Eriko Sugano[‖], Hiroshi Tomita[‖], Tetsuo Takahashi[**], Toru Ishizuka[‡], and Hiromu Yawo[‡§¶1]

From the [‡]Department of Developmental Biology and Neuroscience, Tohoku University Graduate School of Life Sciences, and [¶]Department of Physiology and Pharmacology, Tohoku University Graduate School of Medicine, Sendai 980-8575, [§]Tohoku University Basic and Translational Research Center for Global Brain Science, Sendai 980-8575, [‖]Tohoku University International Advanced Research and Education Organization, Sendai 980-8575, and [**]Faculty of Pharmaceutical Sciences, Toho University, 2-2-1 Miyama, Funabashi-shi, Chiba 274-8510, Japan

A light signal is converted into an electrical one in a single molecule named channelrhodopsin, one of the archaea-type rhodopsins in unicellular green algae. Although highly homologous, two molecules of this family, channelrhodopsin-1 (ChR1) and -2 (ChR2), are distinct in photocurrent properties such as the wavelength sensitivity, desensitization, and turning-on and -off kinetics. However, the structures regulating these properties have not been completely identified. Photocurrents were analyzed for several chimera molecules made by replacing N-terminal segments of ChR2 with the homologous counterparts of ChR1. We found that the wavelength sensitivity of the photocurrent was red-shifted with negligible desensitization and slowed turning-on and -off kinetics when replacement was made with the segment containing the fifth transmembrane helix of ChR1. Therefore, this segment is involved in the determination of photocurrent properties, the wavelength sensitivity, and the kinetics characterizing ChR1 and ChR2. Eight amino acid residues differentiating this segment were exchanged one-by-one, and the photocurrent properties of each targeted mutant ChR2 were further analyzed. Among them, position Tyr^{226}(ChR1)/Asn^{187}(ChR2) is one of the molecular determinants involved in the wavelength sensitivity, desensitization, and turning-on and -off kinetics. It is suggested that these amino acid residues directly or indirectly interact with the chromophore as well as with the protein structure determining the photocurrent kinetics. Some of the chimera channelrhodopsins are suggested to have several advantages over the wild-type ChR2 in the introduction of light-induced membrane depolarization for the purpose of artificial stimulation of neurons *in vivo* and visual prosthesis for photoreceptor degeneration.

Light is perceived by many living organisms on the earth as vital information. In the case of vertebrates, including human beings, the rhodopsins are the molecules involved in the light perception of the photoreceptor cells in the retina (1–3). Each rhodopsin is a seven-pass transmembrane molecule homologous to G-protein-linked receptors and activated by a photoisomerization of a covalently attached chromophore, 11-*cis*-retinal, to all-*trans* configuration. The signal is then transmitted to cyclic GMP phosphodiesterase and reduces the intracellular level of cGMP, which opens the cyclic nucleotide-gated cation channels (4, 5). A light signal is thus converted into an electrical one through a cascade of at least four molecules. On the other hand, during phototactic and photophobic movements of unicellular green algae, light is perceived by archaea-type rhodopsins that are localized in small regions of the plasmalemma covering the eyespot (6–9). Two rhodopsins named channelrhodopsin-1 (ChR1) and -2 (ChR2) were identified in a green alga *Chlamydomonas reinhardtii* and extensively studied (7, 8, 10, 11). Each channelrhodopsin consists of a seven-pass transmembrane apoprotein, channelopsin, and a retinal which covalently binds to the apoprotein. The photoisomerization of all-*trans*-retinal to 13-*cis* configuration is coupled to conformational changes in the protein and causes the permeation of ions. A light signal is thus converted into an electrical one in a single molecule (12). When exogenously expressed in *Xenopus* oocyte, the ChR1 photocurrent was maximally activated at 500 nm (10). Previously, the ChR1 photocurrent was thought to be primarily carried by H^+, but a recent study noted that it was also dependent on other cations (13). On the other hand, the ChR2 photocurrent was preferentially activated at 460 nm and carried by cations like Na^+, K^+, Ca^{2+}, as well as H^+ (11). The photocurrents are also kinetically distinct. The ChR1 photocurrent was hardly desensitized during bright light illumination, although that of ChR2 was rapidly desensitized (10, 11, 14, 18). In this study, we replaced the N-terminal segments of ChR2 with the homologous counterparts of ChR1 and generated several chimeras. These chimeras generated photocurrents showing intermediate properties between ChR1 and ChR2. A possible molecular determinant was identified in the fifth transmembrane helix, which is involved in both the light absorbance and the photocurrent kinetics. Some chimera molecules may

* This work was supported by grants-in-aid for scientific research, Global COE Program (Basic and Translational Research Center for Global Brain Science) and Strategic Research Program for Brain Sciences (SRPBS) from the Ministry of Education, Culture, Sports, Science and Technology (MEXT) of Japan, and Suzuken Memorial Foundation. The costs of publication of this article were defrayed in part by the payment of page charges. This article must therefore be hereby marked "*advertisement*" in accordance with 18 U.S.C. Section 1734 solely to indicate this fact.

[S] The on-line version of this article (available at http://www.jbc.org) contains supplemental data 1–5.

[1] To whom correspondence should be addressed: Dept. of Developmental Biology and Neuroscience, Tohoku University Graduate School of Life Sciences, 2-1 Seiryo-machi, Aoba-ku, Sendai 980-8575, Japan. Tel.: 81-22-717-8150; Fax: 81-22-717-8154; E-mail: yawo@mail.tains.tohoku.ac.jp

be more optimal than ChR2 to depolarize exogenously expressed cells by light.

EXPERIMENTAL PROCEDURES

Plasmid Construction and Expression—The cloning methods of channelopsin1 (chop1) have been described previously (8). Chimeric channelopsins (chops)[2] between chop1 (amino acids 1–345; GenBank™ accession numbers, AB058890/AF385748) and chop2 (amino acids 1–315) (GenBank™ accession number, AB058891/AF461397) with 5′-EcoRI and 3′-BamHI restriction sites were constructed by overlap extension PCR as described previously (15) using KOD plus DNA polymerase (Toyobo, Osaka, Japan). A chimeric chop fragment was obtained, purified, digested by EcoRI and BamHI, and subcloned in-frame into the plasmid pVenus-N1 that has the Venus construct (14). Single amino acid mutants of chop2-(1–315)-Venus were produced using KOD plus mutagenesis kit (Toyobo). Primers used in overlap extension and site-directed mutagenesis are listed in supplemental data 1. Coding regions in all constructed plasmids were fully sequenced to verify that no undesired mutations had been introduced by PCR. HEK293 cells were cultured at 37 °C and 5% CO_2 in Dulbecco's modified Eagle's medium (Sigma) supplemented with 10% fetal bovine serum and transfected using Effectene transfection reagent (Qiagen, Tokyo, Japan) according to the manufacturer's instructions. Twenty four hours post-transfection, the cells were replated onto the collagen-coated glass coverslips and served for the electrophysiology. We did not supplement the culture and experimental media with retinal, but we observed enough large photocurrents for the following experiments.

Measurements of Fluorescence—Cells were prepared for electrophysiological recordings 48 h after transfection. Under conventional confocal microscopy (LSM 510 META, Carl Zeiss, Oberkochen, Germany), Venus was excited at 488 nm, and the fluorescence was obtained with an LP505 emission filter. All the images were captured under fixed conditions such as the laser power and the photomultiplier gain so as to compare the fluorescence distribution among the ChR2 variants. The fluorescence derived from the contour of a cell was automatically detected by an algorithm (supplemental data 2) and then measured in arbitrary fluorescent units. This value was normalized by the number of pixels in the region, and the fluorescence density was obtained.

Electrophysiology—The current-voltage (*I–V*) relationship was examined 48 h after transfection to compare the effective conductance with the membrane protein expression. Other experiments were done 48–96 h after transfection. Fluorescence-labeled isolated cells were identified under conventional epi-fluorescence microscopy (BH2-RFC, Olympus, Tokyo, Japan) equipped with a 60× water-immersion objective (LUMplanPl/IR60x, Olympus). The photocurrents were recorded under the whole-cell patch clamp of a conventional system (Axopatch 200A plus Digdata1200, Molecular Devices Co., Sunnyvale, CA). The standard patch pipette solution contained (in mM), 120 CsOH, 100 glutamate, 50 HEPES, 2.5 MgCl, 2.5 MgATP, 5 Na_2EGTA, 1.2 leupeptin (Sigma), pH 7.4, adjusted by 1 N CsOH. For the analysis of the *I-V* relationship, Cs^+ was replaced by isomolar Na^+. The access resistance was 10–20 megohms and was monitored throughout the recording. The cells were continuously superfused (1–2 ml/min) by standard Tyrode solution (in mM, 138 NaCl, 3 KCl, 1 $CaCl_2$, 1 $MgCl_2$, 10 HEPES, NaOH 4, pH 7.4, by 1 N HCl) or low Na^+ Tyrode solution (in mM, 16 NaCl, 3 KCl, 1 $CaCl_2$, 1 $MgCl_2$, 122 *N*-methyl-D-glucamine, 122 HCl, 10 HEPES, 4 NaOH). The liquid junctional potentials of the sodium glutamate patch pipette were −8 mV at 142 mM Na^+ and −14 mV at 20 mM Na^+ and were corrected. All experiments were performed at room temperature (22–25 °C).

Light Illumination—Three modes of light illumination were used according to the experiments. For the wavelength-response relationship monochromatic light at 400–560 nm (width, 10 nm) of 1-s duration was applied every 20 s under a conventional epifluorescence system equipped with a xenon lamp and electromagnetic shutter (CAM-230, Jasco, Tokyo, Japan). Usually the photocurrent was measured by 2–3 repeats of a protocol, in which the wavelength was changed in the order of 460, 480, 500, 520, 540, 560, 560, 540, 520, 500, 480, 460, 440, 420, 400, 400, 420, 440, and 460 and was averaged for each wavelength. The power density at each wavelength was directly measured by a thermopile (*MIR-100Q*, Mitsubishi Oil Chemicals, Tokyo, Japan), and was (in mW mm^{-2}) 0.021 (400 nm), 0.018 (420 nm), 0.027 (440 nm), 0.027 (460 nm), 0.018 (480 nm), 0.021 (500 nm), 0.015 (520 nm), 0.014 (540 nm), or 0.012 (560 nm), respectively. To investigate the wavelength-response relationship, the amplitude of the peak photocurrent at each wavelength was divided by the power density because there was assumed to be a linear relationship between these values (14). For the *I-V* relationship analysis the xenon lamp light was filtered at 477 ± 10 nm (power density, 1.6 mW mm^{-2}) and was applied for 0.2 s duration every 10 s under a conventional epifluorescence system equipped with an electromagnetic shutter (OSP-3, Olympus). For the analysis of the photocurrent kinetics, we used a blue LED (470 ± 25 nm, LXHL-NB98, Lumileds Lighting Inc., San Jose, CA) regulated by a pulse generator (SEN-7203, Nihon Kohden, Tokyo, Japan) and computer software (pCLAMP 9, Molecular Devices Co.). The maximal power density of LED light was 0.077 mW mm^{-2}.

Data Analysis—The desensitization was quantified as the difference between the peak and the steady-state amplitudes divided by the peak amplitude. The time constants of turning-on (ON) transition (ON time constant, τ_{ON}) were obtained by fitting the photocurrent using the simplex method of nonlinear least squares protocol of the appropriate software (Clampfit 9.2 and 10.1, Molecular Devices Co.). Because the photocurrent was better fitted by two exponential functions after light-off, the effective turning-off (OFF) time constant (τ_{OFF}) was measured as the time to reach e^{-1} (37%) of the steady-state amplitude.

All data in the text are presented as means ± S.E. (number of observations). Mann-Whitney *U* test was used for statistical analysis unless otherwise noted. According to this *p* value, the statistical significance was scored as 0 if $p > 0.05$, as 1 if $0.05 > p > 0.01$, as 2 if $0.01 > p > 0.005$, as 3 if $0.005 > p > 0.001$, as 4

[2] The abbreviations used are: chop, channelopsin; mW, milliwatt; S, siemens; F, farad.

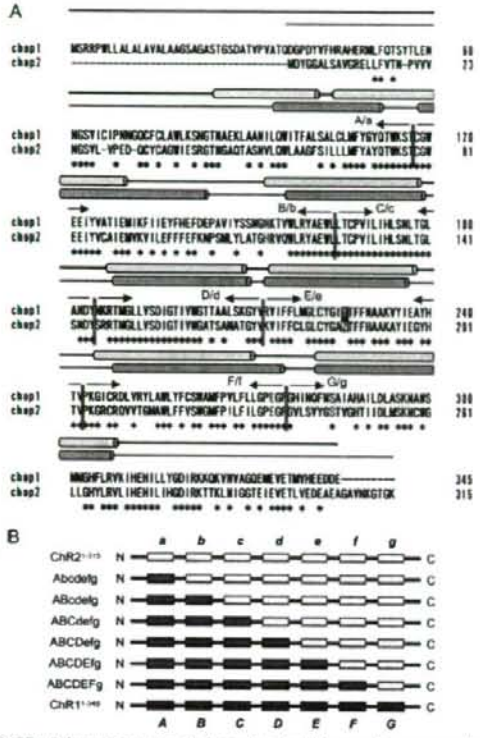

FIGURE 1. **Primary structure of channelopsin chimeras.** *A*, sequence alignment of two channelrhodopsin apoproteins, channelopsin1 (chop1, amino acids 1–345) and channelopsin2 (chop2, amino acids 1–315). The identical amino acids are indicated with an *asterisk*. The putative seven transmembrane domains are indicated by *blue cylinders* (16, 17) or *green cylinders* (8). *Yellow background* indicates the amino acid residues predicted to lie close to retinal. *Crimson letters* indicate the consensus retinal-binding Lys. *Blue letters* indicate the consensus residues defining the Schiff base counterion complex. *Magenta letters* indicate the amino acid residues involved in the retinal-Schiff base binding pocket. *Green letters* indicate the amino acid residues affecting the electron distribution of retinal-Schiff base. Tyr^{226}("E")/Asn^{187}("e"), which are involved in both the wavelength preference and channel gating, are shown by *white letters* with *black background*. *Vertical red double lines* indicate the segment boundaries. The segments are named from the N-terminal as "A" to "G" of chop1 and as "a" to "g" of chop2. *B*, primary constructs of the chimera channelrhodopsins replacing the N-terminal segments of channelrhodopsin2 (ChR2-(1–315)) with homologous counterparts of channelrhodopsin1 (ChR1-(1–345)).

if $0.001 > p > 0.0005$, as 5 if $0.0005 > p > 0.0001$, and as 6 if $p < 0.0001$.

RESULTS

Replacement of N-terminal Segments of ChR2 with Homologous Counterparts of ChR1—Previous studies suggested that ChR1 and -2 have distinct properties, although these apoproteins are highly homologous (Fig. 1*A*). The first to seventh transmembrane domains for each are predicted, although the amino acid sequence involved in the domain was somewhat different among several studies (8, 16, 17). We divided the N-terminal 1–345 amino acids fragment of ChR1 apoprotein (channelopsin1, chop1), which is essential to the photocurrent activation (18), into seven segments so that each, as much as possible, would contain one of the transmembrane domains. These segments are referred to (from N-terminal to C-terminal) as "A," "B," "C," "D," "E," "F," and "G". The homologous counterparts of the essential truncate (1–315 amino acids) of ChR2 apoprotein (channelopsin2, chop2) (11), are referred to as "a," "b," "c," "d," "e," "f," and "g." To identify the segment differentiating the ChR2 photocurrent properties from the ChR1, the N-terminal segments of ChR2-(1–315) were replaced by the homologous counterparts of ChR1-(1–345). We thus made six chimera channelrhodopsins as follows: ChR(Abcdefg), ChR(ABcdefg), ChR(ABCdefg), ChR(ABCDefg), ChR(ABCDEfg), and ChR(ABCDEFg) (Fig. 1*B*).

Membrane Expression—These channelrhodopsins were tagged with one of the green fluorescent protein derivatives, Venus, at their C-terminal ends and expressed in HEK293 cells. Under confocal microscopy, ChR2-(1–315)-Venus fluorescence was distributed preferentially at the contour of the cell, suggesting that it is distributed in the plasma membrane (Fig. 2*A*). Although the fluorescence was weak in the cases of ChR1-(1–345), it was again preferentially distributed at the contour of the cell. The expression was obviously enhanced in any case of chimera channelrhodopsin. As shown in Fig. 2*B*, the fluorescence density in the plasma membrane region was quantified and compared among ChR2-(1–315), ChR1-(1–345), and chimera channelrhodopsins. The fluorescence density of ChR(Abcdefdg) was similar to ChR2, whereas those of ChR(ABcdefg), ChR(ABCdefg), ChR(ABCDefg), and ChR(ABCDEfg) were 150–200% of ChR2. The further "f"-to-"F" exchange significantly reduced the fluorescence density but to a level as great as that of ChR2-(1–315). In contrast, the fluorescence density of ChR1-(1–345) was very small. This result was generally consistent with the immunoblot quantification of membrane-targeted proteins, although the immunoblot density of ChR1-(1–345) was similar to that of ChR(ABCDEFg) (supplemental data 3). **Therefore, the fluorescence density at the contour of the cell would well represent the density of the molecule at the plasma membrane.**

Reevaluation of ChR1 Photocurrent at pH 7.4—Because the ChR1 photocurrent has been studied at pH 4–6 in previous studies (10, 18), its properties at pH 7.4 were re-investigated. Under whole-cell patch clamp at −40 mV, a 1-s light pulse evoked a negative ChR1-(1–345) current with negligible desensitization at wavelengths of 460 and 520 nm (Fig. 3*A*), whereas the same light pulse evoked a ChR2-(1–315) current with a peak and a plateau, both of which were dependent on the wavelength (Fig. 3*B*). For each, the photocurrents were evoked at wavelengths of 400–560 nm. Because the light power was dependent on the wavelength, it was measured directly and was in the range of 0.012–0.027 mW mm^{-2}. The peak photocurrent was almost proportional to the light power density in this small value range (14). The photocurrent sensitivity to each wavelength was thus obtained by dividing the peak photocurrent amplitude by the light power density and normalized to the value at 480 nm. The sensitivity was maximal between 480 and 520 nm in the case of ChR1-(1–345) (Fig. 3*C*). This sensitivity-wavelength relationship was almost identical to the sensitivity-wavelength relationship of ChR1 at pH 7.5 (13). On the other

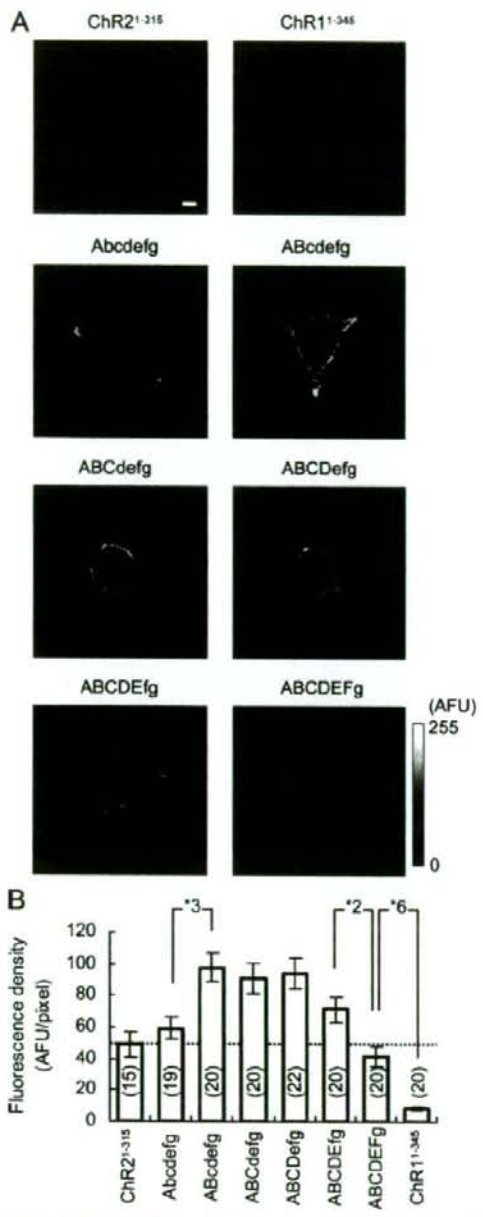

FIGURE 2. **Plasma membrane expression.** *A*, confocal images of the representative HEK293 cells expressing each channelrhodopsins. *Scale bar*, 5 μm. The fluorescence intensity was scaled by the arbitrary fluorescent unit (*AFU*) and expressed in pseudocolor ratings. *B*, average fluorescence densities (mean ± S.E.) at the cell contour of ChR2-(1–315), chimeras and ChR1-(1–345). In this and the following *bar graphs* the number of experiments is in *parentheses*, and the *number with an asterisk* indicates the significance score (Mann-Whitney *U* test).

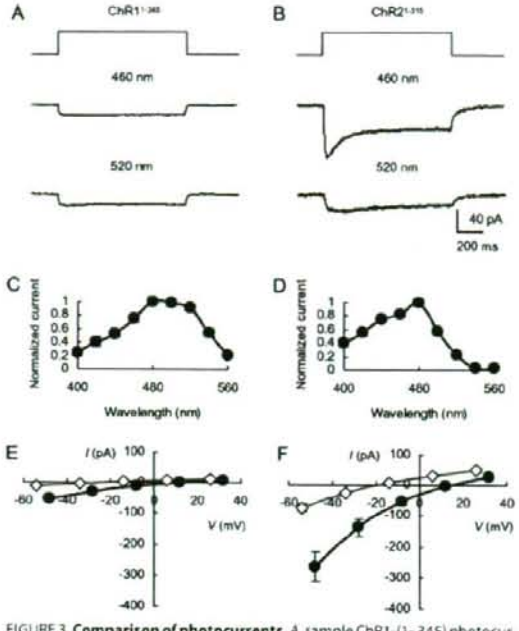

FIGURE 3. **Comparison of photocurrents.** *A*, sample ChR1-(1–345) photocurrent evoked by 1-s pulse illumination (*top*) at 460 nm (*middle*) or 520 nm (*bottom*). *B*, similar to *A*, but a ChR2-(1–315) photocurrent. *C*, wavelength relationship of the ChR1-(1–345) photocurrent ($n = 8$). Mean ± S.E. of normalized currents to 480 nm. *D*, wavelength relationship of the ChR2-(1–315) photocurrent ($n = 8$). *E*, current-voltage (*I-V*) relationships of the ChR1-(1–345) photocurrent at 142 mM $[Na^+]_o$ (*filled circles*, mean ± S.E.) and 20 mM $[Na^+]_o$ (*open diamonds*, mean ± S.E.). *F*, *I-V* relationship of the ChR2-(1–315) photocurrent.

hand, in the case of ChR2-(1–315), the sensitivity at 500–520 was smaller than that at 480 nm (Fig. 3*D*).

The ChR1-(1–345) photocurrents were usually small in comparison with the ChR2-(1–315) as noted in Fig. 3, *A* and *B*. The current-voltage (*I-V*) relationship was investigated for each peak photocurrent evoked by blue light (477 ± 10 nm), which is the wavelength at the maximal sensitivity for both ChR1-(1–345) and ChR2-(1–315), with a pipette solution containing 120 mM Na^+. When the extracellular solution was the standard Tyrode solution containing 142 mM Na^+, the *I-V* relationships of ChR1 and ChR2 were slightly rectified inwardly as shown in Fig. 3, *E* and *F*, *i.e.* the slope conductance at positive membrane potentials was smaller than that at negative membrane potentials. Under close inspection, the ChR2 photocurrent was more rectified than the ChR1 one (supplemental data 4). To evaluate the size of the photocurrent, we estimated the effective conductance as a slope of the *I-V* relationship between −40 and 40 mV divided by the input capacitance of the cell. The mean effective conductance of ChR1-(1–345) was 0.054 ± 0.009 μS/pF ($n = 20$), whereas that of ChR2-(1–315) was 0.228 ± 0.037 μS/pF ($n = 20$) with a significant difference ($p < 0.0001$). The conductance was one of the differences between ChR1-(1–345) and ChR2-(1–315) photocurrent as noted previously (16). Its difference would result partly from the difference of expres-

sion in the plasma membrane (Fig. 2*B*). When the extracellular Na^+ was reduced from 142 to 20 mM, the reversal potential (E_{rev}) of the ChR1-(1–345) peak photocurrent was shifted from 12.6 ± 2.5 to −24.9 ± 2.3 mV (Fig. 3*E*), whereas that of ChR2-(1–315) was shifted from 13.9 ± 1.8 to −21.1 ± 2.0 mV (Fig. 3*F*). As a result the Na^+-dependent shift of E_{rev}, $\Delta E_{rev}(Na^+)$, of ChR1-(1–345) was −37.5 ± 2.2 mV (n = 11), which was similar to that of ChR2-(1–315) (−35.0 ± 1.1 mV, n = 11), and the difference was insignificant. Similar results were obtained when the plateau photocurrents were compared. Therefore, we concluded that ChR1-(1–345) and ChR2-(1–315) are similar in terms of the relative Na^+ permeability to other cations (K^+, H^+, Ca^{2+}, Mg^{2+}, and *N*-methyl-D-glucamine$^+$) at pH 7.4. At pH 6.0, as noted previously (10), the ChR1 photocurrent was large in effective conductance with very positive E_{rev} and showed little dependence on Na^+ (supplemental data 5) as the relative Na^+ permeability of ChR1 is dependent on the pH and is small at low pH (13).

Wavelength-Photocurrent Relationships of the Chimera Channelrhodopsins—The wavelength sensitivity of the photocurrent was similarly investigated for each chimera channelrhodopsin expressed in HEK293 cells. As shown in Fig. 4*A*, each wavelength relationship of the chimera photocurrent was intermediate between ChR1-(1–345) and ChR2-(1–315). For example, in the case of ChR(ABCDEfg), the light sensitivity was maximal at 480 nm, but the photocurrent was more preferably activated at wavelengths 500–540 nm than the wild-type ChR2. The wavelength sensitivity was well quantified by the ratio of the mean photocurrent at 500 and 520 nm to the mean at 440 and 460 nm (G/B ratio) (Fig. 4*B*). Although the significant enhancement of G/B ratio was limited to the exchange of segment "e" of ChR2-(1–315) with "E" ("e"-to-"E" exchange) or "g"-to-"G" exchange, it was significantly greater than that of ChR2-(1–315) but significantly smaller than that of ChR1-(1–345) in chimeras ChR(ABcdefg), ChR(ABCdefg), ChR(ABCDEfg), and ChR(ABCDEFg) ($p < 0.005$).

Ion Permeability of Chimera Channelrhodopsins—The ion permeability was again investigated for each chimera channelrhodopsin by comparing the *I-V* relationships at high Na^+ (142 mM) and low Na^+ (20 mM) extracellular environments (Fig. 5*A*). As summarized in Fig. 5*B*, the $\Delta E_{rev}(Na^+)$ was similar to those of ChR1-(1–345) and ChR2-(1–315) in the cases of ChR(ABcdefg), ChR(ABCdefg), ChR(ABCDefg), ChR(ABCDEfg), and ChR(ABCDEFg). Therefore, these chimera channelrhodopsins are similar to ChR2-(1–315) in terms of the relative Na^+ permeability to other cations (K^+, H^+, Ca^{2+}, Mg^{2+}, and *N*-methyl-D-glucamine$^+$) at pH 7.4. However, the absolute $\Delta E_{rev}(Na^+)$ of ChR(Abcdefg) was significantly smaller than those of the others. It is possible that the permeability of this chimera is less selective to Na^+ and permeable to large cations such as *N*-methyl-D-glucamine$^+$ (11).

The photocurrents of ChR(Abcdefg) and other chimera channelrhodopsins were also less rectified than that of ChR2-(1–315) in their *I-V* relationships (Fig. 5*A*; supplemental data 4). On the other hand as shown in Fig. 5*C*, the effective conductance was variable among chimera channelrhodopsins. It was significantly enhanced by the "b"-to-"B" or "e"-to-"E" exchange, whereas significantly reduced by the "d"-to-"D" or "f"-to-"F" exchange. The effective conductance is dependent on the single channel conductance, the probability of a channel being open and the channel density in the plasma membrane. The results of Fig. 5*C* were consistent with the high fluorescence density at the plasma membrane (Fig. 2*B*) in the cases of ChR(ABcdefg), ChR(ABCdefg), and ChR(ABCDEfg). Therefore, the large effective conductance was partly attributable to the high channel density, although there remains a possibility that other factors are different. Because the effective conductance was smaller than expected from the fluorescence density in the cases of ChR(ABCDefg) and ChR(ABCDEFg), either the single channel conductance or the probability of a channel being open was possibly small in these cases.

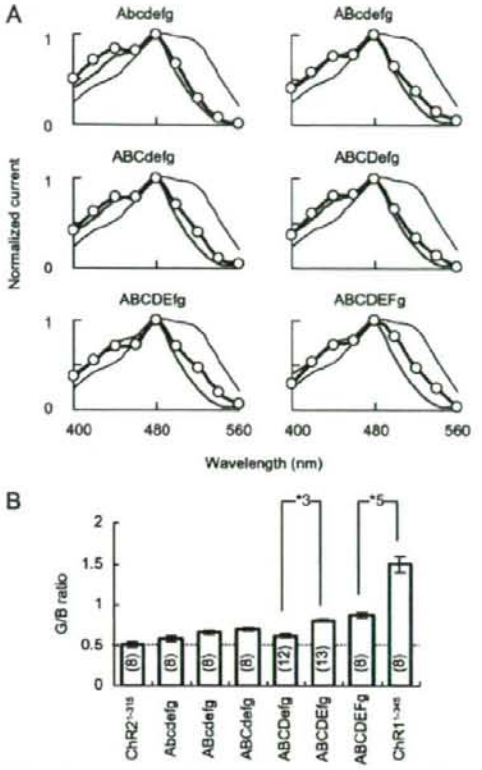

FIGURE 4. **Wavelength sensitivities of chimera photocurrents.** *A*, wavelength-photocurrent relationship of each chimera (*open circles*) is shown in comparison with those of ChR1-(1–345) (*black thin line*) and ChR2-(1–315) (*gray thick line*); ChR(*Abcdefg*), ChR(*ABcdefg*), ChR(*ABCdefg*), ChR(*ABCDefg*), ChR(*ABCDEfg*), and ChR(*ABCDEFg*). *B*, summary of G/B ratio of photocurrents (mean ± S.E.).

Photocurrent Profiles of Chimera Channelrhodopsins—When an LED light was applied as a square pulse, the ChR2-(1–315) photocurrent peaked almost instantaneously, desensitized rapidly to a steady state within 1 s, and turned off rapidly. Because the photocurrent kinetics are dependent on the light intensity, the holding potential as well as pH, the photocurrents of chimera channelrhodopsins were measured at the maximal

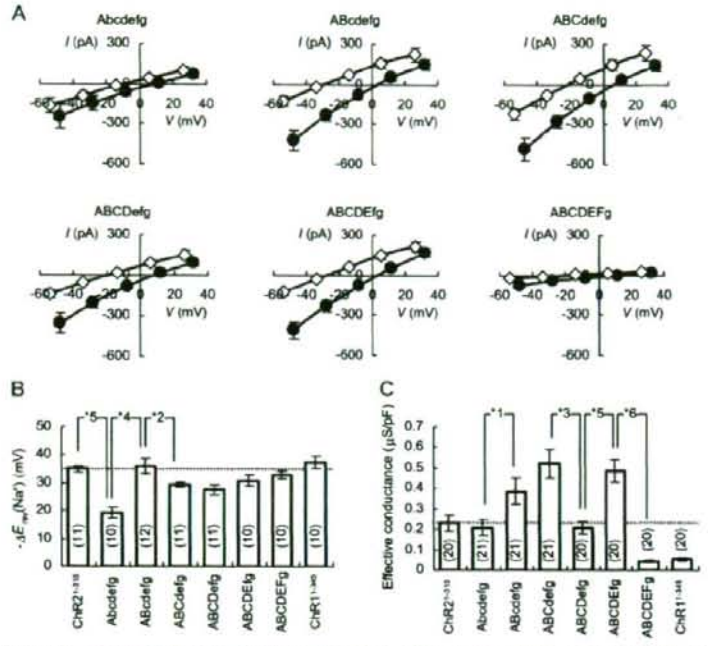

FIGURE 5. **Ion permeability of chimera.** *A*, *I-V* relationship of each chimera (mean ± S.E.). The currents were recorded under environments containing 120 mM $[Na^+]_i$ and 142 mM $[Na^+]_o$ (*filled circles*) or 20 mM $[Na^+]_o$ (*open diamonds*). *B*, summary (mean ± S.E.) of the Na^+-dependent reversal potential shift of each chimera between 142 and 20 mM $[Na^+]_o$. ΔE_{rev}(Na$^+$). *C*, summary (mean ± S.E.) of the effective conductance of each chimera.

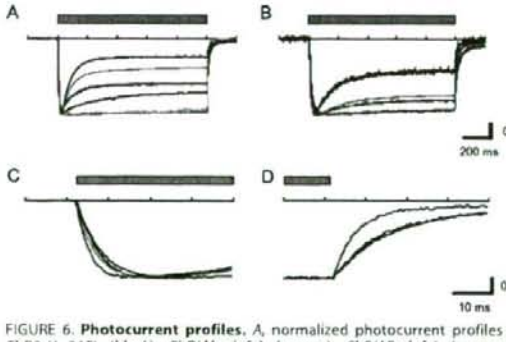

FIGURE 6. **Photocurrent profiles.** *A*, normalized photocurrent profiles of ChR2-(1–315) (*black*), ChR(Abcdefg) (*orange*), ChR(ABcdefg) (*magenta*), ChR(ABCdefg) (*blue*), ChR(ABCDEfg) (*purple*), and ChR1-(1–345) (*brown*) in response to 1-s blue LED illumination at the maximal power density (0.077 mW mm^{-2}). *B*, normalized profiles of integrated photocurrents at wavelengths 400–560 nm. *C*, ON phase of photocurrents normalized to its peak; ChR2-(1–315) (*black*), ChR(Abcdefg) (*orange*), ChR(ABcdefg) (*magenta*), and ChR(ABCDEfg) (*blue*). *D*, OFF phase of the photocurrents normalized to those at the end of illumination; ChR2-(1–315) (*black*), ChR(Abcdefg) (*orange*), ChR(ABcdefg) (*magenta*), and ChR(ABCDEfg) (*blue*).

LED power, at the holding potential of −20 mV and at pH 7.2 inside and pH 7.4 outside of membrane. Although the photocurrents of ChR(Abcdefg), ChR(ABcdefg), ChR(ABCdefg), and ChR(ABCDefg) showed characteristic peak-and-plateau time courses like ChR2-(1–315), they were found to be diverse in their kinetics (Fig. 6*A*). The desensitization of the ChR(Abcdefg) photocurrent was smaller than that of ChR2-(1–315) but larger than that of ChR(ABcdefg) with the maximal LED power. With the progressing replacement of N-terminal segments, the desensitization had a tendency to be further reduced, *e.g.* ChR(ABCDEfg). The magnitude of desensitization was normalized by the peak current and compared among the channelrhodopsins (Fig. 7*A*). The desensitization was significantly reduced by the "a"-to-"A" exchange and was further by "b"-to-"B" exchange. Although the contributions to the desensitization of segments "C/c" and "D/d" were small, "e"-to-"E" exchange significantly reduced the desensitization. The "f"-to-"F" exchange further reduced the desensitization, but to a significantly larger level than that of ChR1. The reduced desensitization of ChR(ABCDEfg), ChR(ABCDEFg), and ChR1-(1–345) may come from the shift of the sensitivity-wavelength relationship. To test this, using the data of Fig. 4*A*, the photocurrents measured at each wavelength from 400 to 560 nm are integrated (Fig. 6*B*), and the desensitization was evaluated on this integrated photocurrent. As shown in Fig. 7*B*, the desensitization of the integrated photocurrent was well correlated to that evoked by the maximal LED power ($r = 0.96$, $p < 0.0005$, paired t test). Therefore, the reduced desensitization cannot be explained by the shift of the sensitivity-wavelength relationship. However, the difference between ChR(ABCDEFg) and ChR1-(1–345) in Fig. 7*A* may be attributed to the different wavelength sensitivity because no obvious difference was observed in the desensitization of the integrated photocurrents (Fig. 7*B*).

These photocurrents were also variable in their turning-on (ON) and turning-off (OFF) kinetics. As shown in Fig. 6, *C* and *D*, where the LED light pulse was applied at its maximal power, the photocurrent of ChR(Abcdefg) was faster than that of ChR2-(1–315) in the ON kinetics, whereas the two were similar in the OFF kinetics. The photocurrent of ChR(ABcdefg) was faster than that of ChR(Abcdefg) in both ON and OFF, whereas that of ChR(ABCDEfg) was similar to ChR2-(1–315) in both ON and OFF. The ON time constant (τ_{ON}) of ChR2 is a function of the LED power, whereas the effective OFF time constant (τ_{OFF}) is not (14). Therefore, the τ_{ON} and τ_{OFF} were both compared at the maximum LED power (Fig. 7, *C* and *D*). The contribution of segment "A/a" to the τ_{OFF} was negligible, whereas both the τ_{OFF} and τ_{ON} became significantly small by replacing

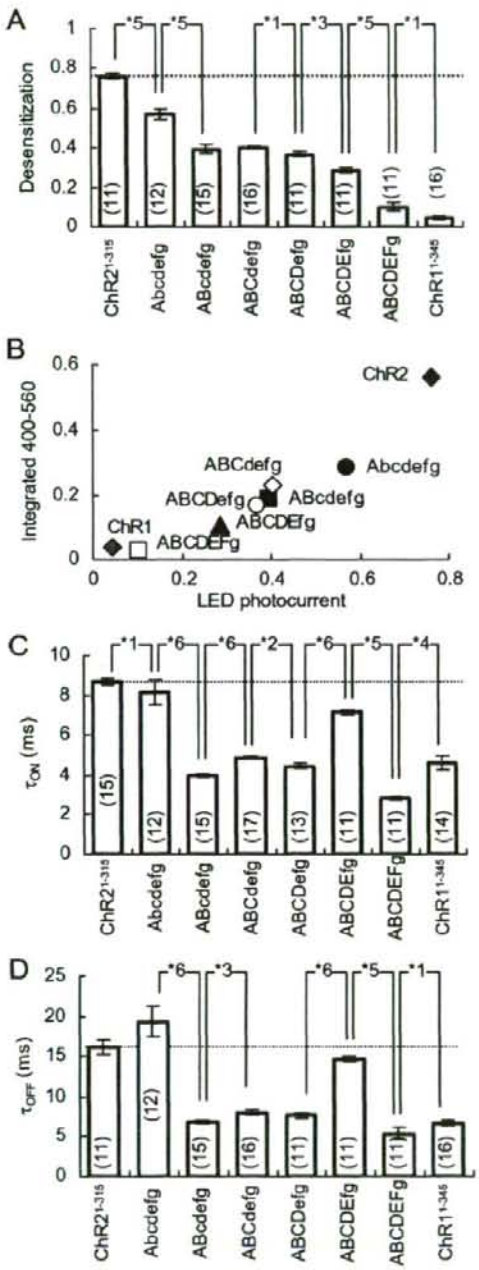

FIGURE 7. **Desensitization, ON, and OFF kinetics.** *A*, magnitude of desensitization was normalized by the peak photocurrent and summarized for channelrhodopsins (mean ± S.E.). *B*, correlation of desensitization between the integrated photocurrent and the LED-evoked photocurrent. *C*, summary of ON time constants (τ_{ON}, mean ± S.E.). *D*, summary of effective OFF time constants (τ_{OFF}, mean ± S.E.).

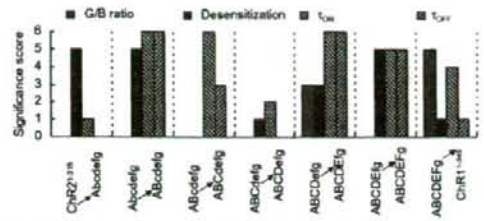

FIGURE 8. **Effects of segment substitution.** The significance scores were compared for four photocurrent properties, the G/B ratio, desensitization, τ_{ON}, and τ_{OFF}, among the segment substitutions (from *left* to *right*) as follows: ChR2-(1–315) *versus* ChR(*Abcdefg*), ChR(Abcdefg) *versus* ChR(*ABcdefg*), ChR(ABcdefg) *versus* ChR(*ABCdefg*), ChR(ABCdefg) *versus* ChR(*ABCDefg*), ChR(ABCDefg) *versus* ChR(*ABCDEfg*), ChR(ABCDEfg) *versus* ChR(*ABCDEFg*), and ChR(ABCDEFg) *versus* ChR1-(1–345).

segment "b" of ChR(Abcdefg) with "B." Although both the τ_{OFF} and τ_{ON} were significantly enlarged by "e"-to-"E" exchange, they were significantly reduced by "f"-to-"F" exchange.

Significance of E-segment as a Determinant of the Photocurrent Properties—The above results indicate that each photocurrent property was variably dependent on the segment exchanges. As shown in Fig. 8, the significance score of the Mann-Whitney *U* test was compared with the photocurrent properties of the G/B ratio, desensitization, and τ_{ON} and τ_{OFF}, and the effects of each single segment exchange were evaluated as follows: from ChR2-(1–315) to ChR(Abcdefg), from ChR(Abcdefg) to ChR(ABcdefg), from ChR(ABcdefg) to ChR(ABCdefg), from ChR(ABCdefg) to ChR(ABCDefg), from ChR(ABCDefg) to ChR(ABCDEfg), from ChR(ABCDEfg) to ChR(ABCDEFg), or from ChR(ABCDEFg) to ChR1-(1–345). Because the "b"-to-"B" and "f"-to-"F" exchanges definitely affected the photocurrent kinetics as well as the effective conductance, these structures may be related to the channel properties. On the other hand, the "g"-to-"G" exchange more definitely influenced the G/B ratio than photocurrent kinetics. We found that all four properties were definitely affected by the "e"-to-"E" exchange. Therefore, it is suggested that segment "E/e" is one of the key determinants of photocurrent properties such as the wavelength sensitivity and the kinetics.

To further test whether the segment "E/e" is sufficient to determine the photocurrent properties, the effect of a single segment exchange from "e" to "E" was investigated. The $\Delta E_{rev}(Na^+)$ of ChR(abcdEfg) was −36.6 ± 3.1 mV (n = 11), which was the same as that of ChR2-(1–315) (−35.0 ± 3.5 mV, n = 11). The effective conductance of ChR(abcdEfg) was 0.173 ± 0.053 μS/pF (n = 20), which was not significantly different from that of ChR2-(1–315). Similar to the case of ChR(ABCDEfg), the light sensitivity was maximal at 480 nm, but there was a preference to 500–540 nm in the case of ChR(abcdEfg). The G/B ratio of ChR(abcdEfg) was 0.85 ± 0.05 (n = 8), which was similar to that of ChR(ABCDEfg) but significantly larger than that of ChR2-(1–315) (Fig. 9). The segments "e" and "E" are different only at eight amino acid residues (Fig. 1*A*). To identify the residues involved in the wavelength preference, we replaced one-by-one each amino acid residue in "e" with the corresponding one of "E" yielding eight channel-

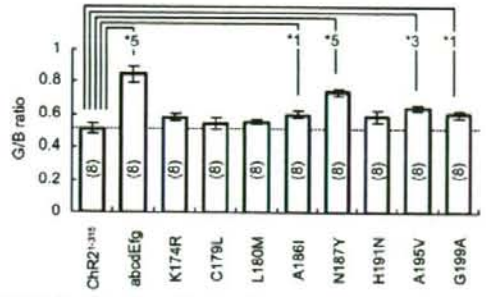

FIGURE 9. **Wavelength sensitivities of E-segment substitutions.** Summary of G/B ratios of photocurrents (mean ± S.E.). The *number with an asterisk* indicates the significance score to ChR2-(1–315) (Mann-Whitney *U* test).

rhodopsins as follows: ChR2(K174R), ChR2(C179L), ChR2-(L180M), ChR2(A186I), ChR2(N187Y), ChR2(H191N), ChR2-(A195V), and ChR2(G199A). The G/B ratio of each amino acid replacement of ChR2-(1–315) is summarized in Fig. 9. The G/B ratio of ChR2(N187Y) was as large as that of ChR(abcdEfg). A small but significantly large G/B ratio was also observed in ChR2(A186I), ChR2(A195V), and ChR2(G199A).

The photocurrent profile of ChR(abcdEfg) was obviously different from those of ChR2-(1–315) (Fig. 10*A*). As summarized in Fig. 10, *B* and *D*, the ChR(abcdEfg) photocurrent was small in the desensitization but large in both the τ_{ON} and τ_{OFF}. The one-by-one amino acid exchanges from "e" to "E" variably changed the photocurrent profile. For example, the desensitization was strongly reduced in ChR2(N187Y) and ChR2(H191N) (Fig. 10*B*). The τ_{ON} was enlarged in ChR2(C179L), ChR2(N187Y), and ChR2(G199A) but reduced in ChR2(L180M) and ChR2(A186I) (Fig. 10*C*). The τ_{OFF} was strongly enlarged in ChR2(N187Y) but reduced in ChR2(L180M) and ChR2(A186I) (Fig. 10*D*).

To evaluate the effects of the amino acid exchanges, the statistical significance was scored according to the *p* value of the Mann-Whitney *U* test as done previously. Fig. 11*A* summarizes the significance scores of the single segment and the single amino acid exchanges from "e" to "E." We found that all four photocurrent properties, the G/B ratio, desensitization, τ_{ON}, and τ_{OFF}, were definitely affected by the single segment exchange from ChR2-(1–315) to ChR(abcdEfg). These properties were also definitely changed in ChR2(N187Y). The ChR2(N187Y) resembled ChR(abcdEfg) in all four properties.

The above results suggest that the position Tyr^{226}("E")/Asn^{187}("e") is one of the possible determinants of the wavelength dependence of the photocurrent. To test this, we examined the wavelength sensitivity of a targeted mutant of ChR1-(1–345), ChR1(Y226N), in which Tyr^{226} of ChR1-(1–345) was replaced with Asn. As shown in Fig. 12*A*, this mutation blue-shifted the wavelength-photocurrent relationship toward that of ChR2-(1–315). The G/B ratio of ChR1(Y226N) was 0.97 ± 0.06 ($n = 8$), which was significantly smaller than that of ChR1-(1–345) (Fig. 12*B*). The ChR1(Y226N) was also different from ChR1-(1–345) in the photocurrent kinetics (Fig. 12*C*), the enhancement of desensitization (Fig. 12*D*), the elongation of τ_{ON} (Fig. 12*E*), and the reduction of τ_{OFF} (Fig. 12*F*).

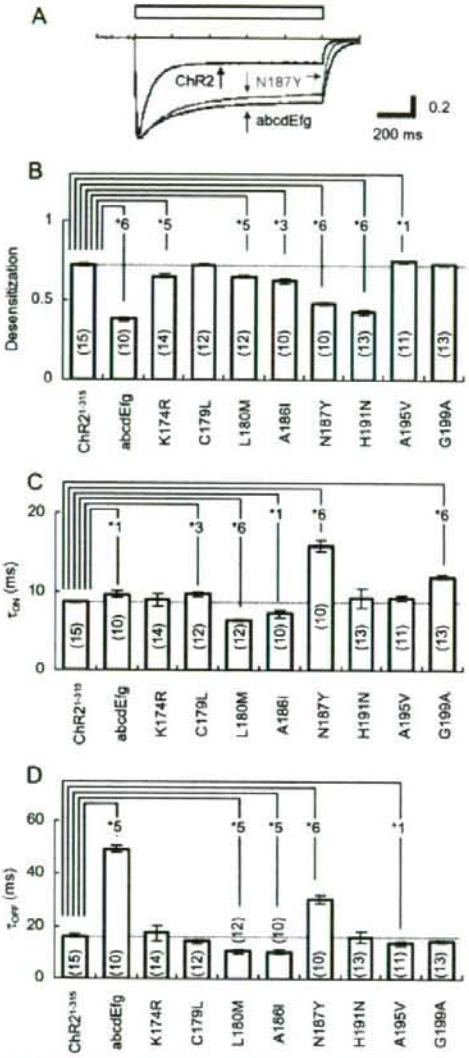

FIGURE 10. **Photocurrent kinetics of E-segment substitutions.** *A*, normalized photocurrent profiles of ChR2-(1–315) (*black line*), ChR(abcdEfg) (*black line*), and ChR2(N187Y) (*gray line*) in response to 1-s blue LED illumination at the maximal power. *B*, summary of photocurrent desensitization (mean ± S.E.). *C*, summary of τ_{ON} (mean ± S.E.). *D*, summary of τ_{OFF} (mean ± S.E.).

DISCUSSION

Molecular Determinants Differentiating ChR2 from ChR1—In this study we divided ChR2-(1–315) into seven segments, "a" to "g," so that each segment contained one of the seven putative transmembrane domains. By replacing the N-terminal segments of ChR2-(1–315) with the homologous counterparts of ChR1-(1–345), "A" to "F," we identified the structure differentiating ChR2 from ChR1. The G/B ratio of the photocurrent,

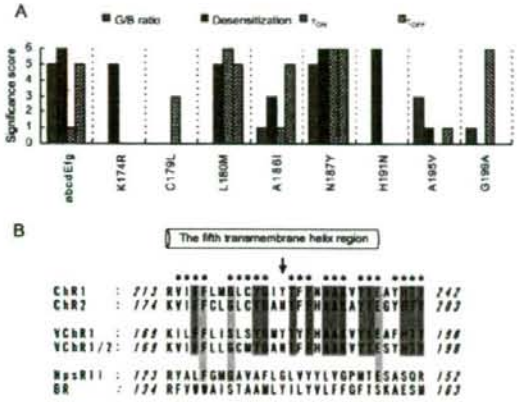

FIGURE 11. **Effects of E-segment substitutions.** *A*, significance scores were compared for four photocurrent properties, the G/B ratio, desensitization, τ_{ON} and τ_{OFF} among E-segment substitutions. *B*, alignment of the fifth transmembrane domain sequences from ChR1, ChR2, and their phylogenic relatives: channelrhodopsins from *V. carteri* (VChR1 and VChR1/2), sensory rhodopsin II from *N. pharaonis* (NpsRII), and bacteriorhodopsin from *H. salinarum* (BR). The putative fifth transmembrane domain is indicated by the *cylinder*. The identical amino acids between ChR1 and ChR2 are indicated with an *asterisk*. *Gray background*, the amino acid residues conserved among four channelrhodopsins, ChR1, ChR2, VChR1, and VChR1/2. *Ash background*, the amino acid residues conserved among ChR1, ChR2, and NpsRII. The *arrow* indicates Tyr^{226}(ChR1)/Asn^{187}(ChR2) position.

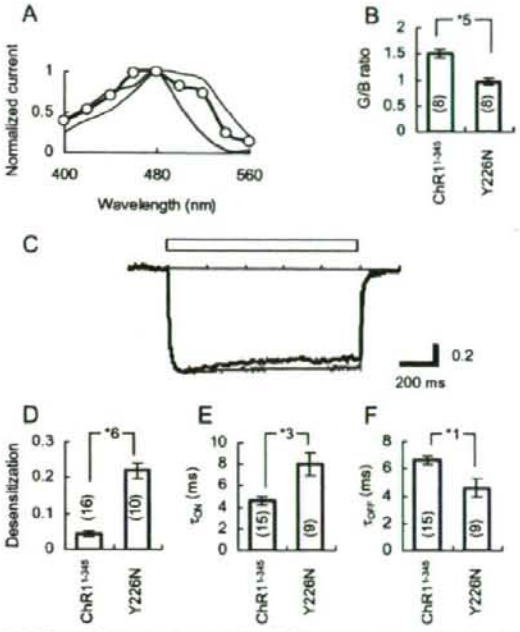

FIGURE 12. **Photocurrent properties of ChR1(Y226N).** *A*, wavelength relationship of ChR1(Y226N) (*open circles*) is shown in comparison with those of ChR1-(1–345) (*black thin line*) and ChR2-(1–315) (*gray thick line*) photocurrents. *B*, summary of the effect of Y226N exchange on the G/B ratio. *C*, normalized photocurrent profiles of ChR1-(1–345) (*gray*) and ChR1(Y226N) (*black*) in response to 1-s blue LED illumination at the maximal power density (0.077 mW mm^{-2}). The time scale is 200 ms/division. The effect of Y226N exchange was summarized on the desensitization (*D*), τ_{ON} (*E*), and τ_{OFF} (*F*) of photocurrents (mean ± S.E.).

used to evaluate the wavelength preference, was gradually increased with the replacements of the N-terminal segments, "A/a" to "C/c," and further by the "e"-to-"E" replacement. But the effect of the "g"-to-"G" replacement was the most definitive, suggesting that the seventh transmembrane helix has structures involved in the color tuning of the molecule. Previously, ChR1 and ChR2 have been differentiated in the relative permeability of Na^+ (10, 11). However, as the cation selectivity of ChR1 photocurrent is dependent on the pH, the photocurrent is less dependent on Na^+ at low pH (13). Consistent with this notion, we did not find any difference in the ion selectivity at pH 7.4. On the other hand, they were differentiated by the effective conductance as noted previously (16). The effective conductance was large even when the first five segments "a" to "e" of ChR2-(1–315) were replaced by "A" to "E" of ChR1-(1–345). The large effective conductance of this chimera channelrhodopsin was in part attributable to the expression level in the plasma membrane. However, further "f"-to-"F" replacement reduced the effective conductance to as small as that of ChR1-(1–345). This is somewhat inconsistent with the fluorescence density of these molecules in the plasma membrane. The "F/f" segment itself or its interaction with other segments is likely to be involved in the regulation of channel conductance or probability of a channel being open. We profiled the photocurrent kinetics by three quantities, the desensitization, τ_{ON}, and τ_{OFF}. Although variable, the chimeras ChR(Abcdefg), ChR(ABcdefg), ChR(ABCdefg), ChR(ABCDefg), and ChR(ABCDEfg) generated photocurrents with properties kinetically intermediate between ChR1-(1–345) and ChR2-(1–315). On the other hand, the chimera ChR(ABCDEFg) was kinetically more similar to ChR1-(1–345). Taken together, the properties differentiating the photocurrent kinetics of ChR1 from those of ChR2 are not confined to a specific structure, but are variably influenced by the exchange of each segment. Even the exchanges of the "C/c" and "D/d" segments definitely changed the photocurrent properties, although the third and the fourth transmembrane domains are highly conserved among channelrhodopsins (16, 17). This is consistent with the notion that these domains are also involved in the channel properties of ChR2-(1–315), and indeed, the single amino acid mutation H134*R* enhanced the photocurrent amplitude (19). In this study we further investigated the "E/e" segment because it definitely changed the photocurrent properties without reducing the effective conductance.

Fifth Transmembrane Helix as the Determinant of Wavelength Sensitivity—In relation to other archaea-type rhodopsins, interactions between the retinal chromophore and its protein environment are the determinants of the wavelength preferences. Three factors are suggested to be involved in these interactions (20, 21) as follows: (i) the strength of the protein environment forcing the retinal to be a coplanar 6*s*-*trans* conformation; (ii) the protein environment electrically interacting with the chromophore with its counter ion or hydrogen bond acceptor; and (iii) a less well defined long range coupling, which

is thought to involve the interaction of polar or polarizable amino acid groups with the chromophore, influencing the stability of the ground state. The amino acid residues assumed to be related to these interactions are mostly present from the third to the seventh transmembrane domains (22, 23) and are almost conserved between ChR1 and ChR2 (Fig. 1), *e.g.* the consensus retinal-binding residue, Lys^{296}("G" segment)/Lys^{257}("g" segment) in the seventh transmembrane domain; the consensus residues defining the Schiff base counterion complex, Arg^{159}("B")/Arg^{120}("b") and Glu^{162}("B")/Glu^{123}("b") in the third transmembrane domain; and Asp^{292}("G")/Asp^{253}("g") in the seventh transmembrane domain, which are critical for the wavelength preference (17, 24, 25). The nonpolar amino acid residues involved in the retinal-Schiff base binding pocket, Gly^{220}("E")/Gly^{181}("e"), Leu^{221}("E")/Leu^{182}("e"), and Cys^{222}("E")/Cys^{183}("e") in the fifth transmembrane domain, which are predicted to be closely located to the β-ionone ring of retinal, are all conserved between ChR1 and ChR2 (17). Other amino acid residues that affect the electron distribution of the retinal-Schiff base are Asn^{153}("B")/His^{114}("b"), Glu^{274}("F")/Glu^{235}("f"), and Ser^{284}("G")/Ser^{245}("g"). However, the wavelength sensitivity of the chimera was only minimally changed by the "b"-to-"B" exchange. On the other hand, the single "e"-to-"E" exchange of ChR2-(1–315) red-shifted the wavelength sensitivity of the photocurrent, and the single "E"-to-"e" exchange of ChR(ABCDEfg) blue-shifted it. This indicates the presence of another structure either regulating the electron distribution of the retinal-Schiff base or interacting with it through long range coupling. The results of our experiments using ChR2(N187Y) and ChR1(Y226N) indicate that one-by-one amino acid replacement of Asn^{187}("e") to the corresponding Tyr red-shifted the sensitivity-wavelength relationship, whereas the reverse replacement of Tyr^{226}("E") to Asn blue-shifted it. The position of Tyr^{226}("E")/Asn^{187}("e") would lie adjacent to the nonpolar retinal binding pocket if the α-helix structure is predicted for the fifth transmembrane domain. It is possible that these amino acid residues have some additional interaction with retinal. The hydroxyl-bearing Tyr^{226} would probably interact preferentially with the excited-state charge distribution around the β-ionone ring of retinal to lower the excitation energy and red-shift the absorption spectrum (26, 27). Alternatively, these residues may interact with retinal-Schiff base with long range coupling.

An alignment of the motif corresponding to the fifth transmembrane helix domain for ChR1 and ChR2 is shown in Fig. 11*B*, in comparison with the other phylogenic relatives. The recently identified channelrhodopsins from *Volvox carteri*, VChR1 (17) and VChR1/2 (28), are highly homologous to both ChR1 and ChR2. Of 18 amino acids conserved between ChR1 and ChR2, 12 are found in both VChR1 and VChR1/2, 4 are found only in VChR1/2, and 1 is found only in VChR1. The counterpart of Tyr^{226}(ChR1)/Asn^{187}(ChR2) is Asn in the case of blue-absorbing VChR1/2, whereas it is Tyr in the case of more red-shifted VChR1. Although this is consistent with the present result that Asn-to-Tyr replacement red-shifted the absorption spectrum, the involvement of other amino acid residues should not be excluded. On the other hand, the sequences of sensory rhodopsin II from *Natronobacterium pharaonis* (the maximum absorption at 500 nm) and bacteriorhodopsin from *Halobacterium salinarum* (the maximum absorption at 550 nm) are less homologous in this region. Of 18 amino acids conserved between ChR1 and ChR2, 3 are found only in sensory rhodopsin II and 0 in bacteriorhodopsin. It is thus possible that the color-tuning contribution of the fifth transmembrane domain is different in these prokaryotic rhodopsins.

Fifth Transmembrane Helix as the Determinant of Photocurrent Kinetics—The "E/e" segment, which contains the fifth transmembrane helix, was also one of the structural determinants of the photocurrent kinetics. When the "e"-to-"E" exchange was made on chimera ChR(ABCDefg), the desensitization was reduced, whereas both the τ_{ON} and τ_{OFF} were definitely enlarged. It was also the case when the same exchange was made on ChR2-(1–315). Therefore, the photocurrent kinetics such as desensitization, τ_{ON}, and τ_{OFF} are dependent on the structure intrinsic to the "E/e" segment. In the "E/e" segment the amino acid residue Tyr^{226}("E")/Asn^{187}("e") again was central in determining the photocurrent kinetics. The desensitization was strongly reduced in ChR2(N187Y) and ChR2(H191N), whereas it was enhanced by Y226N exchange of ChR1-(1–345). However, it was also dependent on other structural components such as the "A/a" and "B/b" segments. The τ_{OFF} was definitely enhanced in ChR2(N187Y) but reduced in ChR2(L180M) and ChR2(A186I). The Y226N exchange of ChR1-(1–345) also reduced τ_{OFF}. It is thus suggested that the position Tyr^{226}("E")/Asn^{187}("e") is involved in the channel closure but that the interaction with other key residues is important. However, both the N187Y exchange of ChR2-(1–315) and the Y226N exchange of ChR1-(1–345) elongated τ_{ON}. Because τ_{ON} is dependent on the light intensity (14) but is also expected to be dependent on τ_{OFF} as a consequence of the photocycle response (18, 28, 29), further studies are necessary to reveal the variability of this value.

Conclusion—This work revealed the significance of the fifth transmembrane helix, particularly its residue Tyr^{226}(ChR1)/Asn^{187}(ChR2), as a molecular determinant differentiating the photocurrent properties between ChR1 and ChR2. Chimeric mutation by a segment exchange has been a powerful tool for identifying the molecular determinants involved in a certain function. For the first time, this study made a series of chimeric mutations by replacing the molecular segments containing each transmembrane helix of ChR2 with the homologous counterparts of ChR1. Based on systematic and quantitative studies of the distribution of the molecules, wavelength sensitivity, reversal potential, and kinetic profile, it is suggested that the fifth transmembrane helix is involved in both the wavelength sensitivity and the kinetic profile of the photocurrent. Moreover, all these results strongly suggest that the residue Tyr^{226}("E")/Asn^{187}("e") lies at a key position enabling it to interact with the retinal-Schiff base. It also lies at a position interacting with other residues involved in the photocurrent kinetic profiles such as desensitization, τ_{ON}, and τ_{OFF}. The significance of Tyr^{226}("E")/Asn^{187}("e") has to be further investigated by mutations replacing Asn^{187} of ChR2-(1–315) with various amino acid residues and/or by x-ray crystallographic analysis (20, 30).

Recently the ChR2-mediated photostimulation of neurons has been applied to investigate the function of neural networks *in vivo* (31–34). Moreover, ChR2-expressing transgenic animals have been generated that are successfully used to study the neural basis of behavioral responses in *Caenorhabditis elegans* (19), zebrafish (35), and mammals (36). Given its superiority in spatio-temporal resolution, ChR2 has become a powerful tool for the investigation of neural networks.

ChR2 is also a potential tool as a visual prosthesis for photoreceptor degeneration (37). In retinal degenerative diseases such as retinitis pigmentosa, photoreceptor cells are lost while preserving the inner retinal neurons such as retinal ganglion cells and bipolar cells. Exogenous expression of ChR2 in these neurons using viral vectors (38, 39) or *in vivo* electroporation methods (40) restores visually evoked responses in the visual cortex of rodents.

However, some further technological developments are necessary to achieve the full potential of ChR2. First, photosensitive channels with various wavelength sensitivities are desirable. One of the *Volvox*-derived channelrhodopsins, VChR1, may be a candidate because it has a peak absorbance at 540 nm (17). Second, the small single channel conductance of ChR2 (in the magnitude of fS) (12, 37) should be compensated by facilitating the membrane expression. Alternatively, it would be useful to develop a ChR2 with increased single channel conductance. Third, the prominent desensitization of ChR2 photocurrent limits its application for repetitive stimulation at high frequency. This could be overcome by reducing the desensitization or facilitating the recovery rate.

Some of the chimera channelrhodopsins have several advantages over the wild-type ChR2 in applying to the light-induced membrane depolarization (14, 31, 41). For example, the chimera ChR(ABCDEfg) is sensitive to wavelengths of 480–540 nm, has large effective conductance when expressed in HEK293 cells, and its photocurrent desensitization was almost negligible. Moreover, its ON and OFF kinetics were the same as those of ChR2. Therefore, this chimera, to which we give the name "channelrhodopsin/wide receiver," would become a good tool to stimulate neurons repetitively with low intensity flash light and also a potential tool as a visual prosthesis of photoreceptor degeneration (38, 39). Another potentially useful chimera is ChR(ABcdefg) because it is very fast in both its ON and OFF kinetics. It is also characterized by small desensitization and large effective conductance. This chimera, to which we give the name "channelrhodopsin/fast receiver," would become a good tool to stimulate neurons repetitively at high frequency flash. The application of channelrhodopsins would be facilitated by this new lineup of chimeras.

Acknowledgments—We thank Dr. G. Nagel (Universität Würzberg, Würzberg, Germany) for ChR2 apoprotein cDNA; Dr. A. Miyawaki (RIKEN BSI, Wako-shi, Japan) for Venus cDNA; Dr. M. Wakamori (Tohoku University, Sendai, Japan) for an HEK293 cell line; Dr. K. Miyazaki for measuring the light power density of instruments; Dr. H. Kataoka for comments on the manuscript, and B. Bell for language assistance.

REFERENCES

1. Nathans, J., Thomas, D., and Hogness, D. S. (1986) *Science* **232,** 193–202
2. Nathans, J. (1999) *Neuron* **24,** 299–312
3. Palczewski, K. (2006) *Annu. Rev. Biochem.* **75,** 743–767
4. Kaupp, U. B., and Seifert, R. (2002) *Physiol. Rev.* **82,** 769–824
5. Bradley, J., Reisert, J., and Frings, S. (2005) *Curr. Opin. Neurobiol.* **15,** 343–349
6. Melkonian, M., and Robenek, H. (1980) *J. Ultrastruct. Res.* **72,** 90–102
7. Sineshchekov, O. A., Jung, K.-H., and Spudich, J. L. (2002) *Proc. Natl. Acad. Sci. U. S. A.* **99,** 8689–8694
8. Suzuki, T., Yamasaki, K., Fujita, S., Oda, K., Iseki, M., Yoshida, K., Watanabe, M., Daiyasu, H., Toh, H., Asamizu, E., Tabata, S., Miura, K., Fukuzawa, H., Nakamura, S., and Takahashi, T. (2003) *Biochem. Biophys. Res. Commun.* **301,** 711–717
9. Kateriya, S., Nagel, G., Bamberg, E., and Hegemann, P. (2004) *News Physiol. Sci.* **19,** 133–137
10. Nagel, G., Ollig, D., Fuhrmann, M., Kateriya, S., Musti, A. M., Bamberg, E., and Hegemann, P. (2002) *Science* **296,** 2395–2398
11. Nagel, G., Szellas, T., Huhn, W., Kateriya, S., Adeishvili, N., Berthold, P., Ollig, D., Hegemann, P., and Bamberg, E. (2003) *Proc. Natl. Acad. Sci. U. S. A.* **100,** 13940–13945
12. Hegemann, P. (2008) *Annu. Rev. Plant. Biol.* **59,** 167–189
13. Berthold, P., Tsunoda, S. P., Ernst, O. P., Mages, W., Gradmann, D., and Hegemann, P. (2008) *Plant Cell* **20,** 1665–1677
14. Ishizuka, T., Kakuda, M., Araki, R., and Yawo, H. (2006) *Neurosci. Res.* **54,** 85–94
15. Sambrook, J., and Russell, D. W. (2001) *Molecular Cloning: A Laboratory Manual,* 3rd Ed., pp. 13.36–13.39, Cold Spring Harbor Laboratory Press, Cold Spring Harbor, NY
16. Nagel, G., Szellas, T., Kateriya, S., Adeishvili, N., Hegemann, P., and Bamberg, E. (2005) *Biochem. Soc. Trans.* **33,** 863–866
17. Zhang, F., Prigge, M., Beyrière, F., Tsunoda, S. P., Mattis, J., Yizhar, O., Hegemann, P., and Deisseroth, K. (2008) *Nat. Neurosci.* **11,** 631–633
18. Hegemann, P., Ehlenbeck, S., and Gradmann, D. (2005) *Biophys. J.* **89,** 3911–3918
19. Nagel, G., Brauner, M., Liewald, J. F., Adeishvili, N., Bamberg, E., and Gottschalk, A. (2005) *Curr. Biol.* **15,** 2279–2284
20. Luecke, H., Schobert, B., Lanyi, J. K., Spudich, E. N., and Spudich, J. L. (2001) *Science* **293,** 1499–1503
21. Shimono, K., Hayashi, T., Ikeura, Y., Sudo, Y., Iwamoto, M., and Kamo, N. (2003) *J. Biol. Chem.* **278,** 23882–23889
22. Pebay-Peyroula, E., Royant, A., Landau, E. M., and Navarro, J. (2002) *Biochim. Biophys. Acta* **1565,** 196–205
23. Adamian, L., Ouyang, Z., Tseng, Y. Y., and Liang, J. (2006) *Photochem. Photobiol.* **82,** 1426–1435
24. Kloppmann, E., Becker, T., and Ullmann, M. (2005) *Proteins* **61,** 953–965
25. Hoffmann, M., Wanko, M., Strodel, P., König, P. H., Frauenheim, T., Schulten, K., Thiel, W., Tajkhorshid, E., and Elstner, M. (2006) *J. Am. Chem. Soc.* **128,** 10808–10818
26. Kochendoerfer, G. G., Lin, S. W., Sakmar, T. P., and Mathies, R. A. (1999) *Trends Biochem. Sci.* **24,** 300–305
27. Hillebrecht, J. R., Galan, J., Rangarajan, R., Ramos, L., McCleary, K., Ward, D. E., Stuart, J. A., and Birge, R. R. (2006) *Biochemistry* **45,** 1579–1590
28. Ernst, O. P., Sánchez Murcia, P. A., Daldrop, P., Tsunoda, S. P., Kateriya, S., and Hegemann, P. (2008) *J. Biol. Chem.* **283,** 1637–1643
29. Bamann, C., Kirsch, T., Nagel, G., and Bamberg, E. (2008) *J. Mol. Biol.* **375,** 686–694
30. Miyazawa, A., Fujiyoshi, Y., and Unwin, N. (2003) *Nature* **423,** 949–955
31. Li, X., Gutierrez, D. V., Hanson, M. G., Han, J., Mark, M. D., Chiel, H., Hegemann, P., Landmesser, L. T., and Herlitze, S. (2005) *Proc. Natl. Acad. Sci. U. S. A.* **102,** 17816–17821
32. Petreanu, L., Huber, D., Sobczyk, A., and Svoboda, K. (2007) *Nat. Neurosci.* **10,** 663–668
33. Huber, D., Petreanu, L., Ghitani, N., Ranade, S., Hromadka, T., Mainen, Z., and Svoboda, K. (2008) *Nature* **451,** 61–64
34. Kuhlman, S. J., and Huang, Z. J. (2008) *PLoS ONE* **3,** e2005

35. Douglass, A. D., Kraves, S., Deisseroth, K., Schier, A. F., and Engert, F. (2008) *Curr. Biol.* **18,** 1133–1137
36. Arenkiel, B. R., Peca, J., Davison, I. G., Feliciano, C., Deisseroth, K., Augustine, G. J., Ehlers, M. D., and Feng, G. (2007) *Neuron* **54,** 205–218
37. Herlitze, S., and Landmesser, L. T. (2007) *Curr. Opin. Neurobiol.* **17,** 87–94
38. Bi, A., Cui, J., Ma, Y. P., Olshevskaya, E., Pu, M., Dizhoor, A. M., and Pan, Z. H. (2006) *Neuron* **50,** 23–33
39. Tomita, H., Sugano, E., Yawo, H., Ishizuka, T., Isago, H., Nankawa, S., Kügler, S., and Tamai, M. (2007) *Investig. Ophthalmol. Vis. Sci.* **48,** 3821–3826
40. Lagali, P. S., Balya, D., Awatramani, G. B., Munch, T. A., Kim, D. S., Busskamp, V., Cepko, C. L., and Roska, B. (2008) *Nat. Neurosci.* **11,** 667–675
41. Boyden, E. S., Zhang, F., Bamberg, E., Nagel, G., and Deisseroth, K. (2005) *Nat. Neurosci.* **8,** 1263–1268

CELL STRUCTURE AND FUNCTION 33: 21–26 (2008)

BDNF Increases the Phagocytic Activity in Cultured Iris Pigment Epithelial Cells

Hikari Yoshida[1], Hiroshi Tomita[2*], Eriko Sugano[2,3], Hitomi Isago[2], Sei-ichi Ishiguro[4], and Makoto Tamai[2]

[1]Department of Ophthalmology, Tohoku University School of Medicine, Sendai, Japan, [2]Department of Biofunctional Science, Tohoku University Biomedical Engineering Research Organization, Sendai, Japan, [3]Department of Biofunctional Science, Tohoku University International Advanced Research and Education Organization, Sendai, Japan, and [4]Department of Biochemistry and Biotechnology, Hirosaki University, Hirosaki, Japan

ABSTRACT. **To investigate the effect of brain derived neurotrophic factor (BDNF) on the phagocytic activity in iris pigment epithelial (IPE) cells, purified porcine photoreceptor outer segments (POS) were applied to cultured IPE cells for three hours. To measure phagocytic activities, bound and total POS were differentially stained using a double immunofluorescence staining method. BDNF increased the binding of POS in IPE cells in a dose-dependent manner. Ingestion of POS, however, was not affected throughout the concentrations used in this study. To investigate the signal transduction pathways of BDNF, a phosphatidylinositol 3-kinase (PI3K) inhibitor, LY294002, and MAPK/ERK kinase (MEK) inhibitor, PD98059, were used for this study. LY294002 had no effect on the binding and ingestion of POS in BDNF-treated IPE cells. On the other hand, PD98059 completely inhibited the increase of POS binding in BDNF-treated cells and also decreased the ingestion of POS. These results indicate that increased POS binding activity by BDNF and the decreased ingestion of POS were mediated through the MAPK pathway.**

Key words: brain-derived neurotrophic factor/iris pigment epithelial cells/mitogen-activated protein kinase/phagocytosis/retina

Introduction

One of the specialized functions in retinal pigment epithelial (RPE) cells is the phagocytosis of photoreceptor outer segments (POS) (Young, 1967; Young and Bok, 1969). The phagocytic process consists of three phases: binding, ingestion, and digestion of POS. Dysfunction of these processes causes photoreceptor degeneration (Bok and Hall, 1971; Herron *et al.*, 1969; LaVail and Battelle, 1975). It is known that Royal College Surgeon (RCS) rats have normal function in the binding phase of POS, but they show abnormality in the ingestion phase (Chaitin and Hall, 1983). Recently, the mutation of receptor tyrosine kinase, MertK, was found in RCS rats (Feng *et al.*, 2002).

It has been reported that various neurotrophic factors, growth factors, and cytokines have protective effects against neuronal degenerations (Lindsay, 1994; Tomita *et al.*, 1999). Specifically, brain-derived neurotrophic factor (BDNF) plays an important role in the protection of retinal degeneration such as ischemic injury (Kano *et al.*, 2002; Unoki and LaVail, 1994), excitotoxicity (Rocha *et al.*, 1999), axotomy (Peinado-Ramon *et al.*, 1996; Watanabe *et al.*, 1997) and light damage (LaVail *et al.*, 1992).

We have researched the substitution of iris pigment epithelial (IPE) cells for RPE cells for the treatment of patients with age-related macular degeneration (AMD) because IPE cells are of the same embryonic origin as RPE cells (Abe *et al.*, 2000a; Abe *et al.*, 1999a; Abe *et al.*, 1999b; Abe *et al.*, 2000b). We have previously reported that IPE cells possess phagocytic activity for POS, which is about 70% of RPE cells. However, phagocytic activities of IPE cells were increased up to those of RPE cells by using a basic fibroblast growth factor (bFGF) gene transfer (Sakuragi *et al.*, 2001). Transplantation of BDNF or bFGF gene transferred IPE cells into the subretinal space have a protective effect against photoreceptor degeneration in rats (Kano *et al.*, 2002).

*To whom correspondence should be addressed: Hiroshi Tomita, Department of Biofunctional Science, Tohoku University Biomedical Engineering Research Organization, 2-1 Seiryomachi, Aobaku, Sendai, 980-8575, Japan.
Tel: +81-22-717-7295, Fax: +81-22-717-7295
E-mail: hiroshi-tomita@tubero.tohoku.ac.jp

In our present work, we investigated the effect of BDNF on phagocytic activity in IPE cells and their signal transduction pathways.

Methods and Materials

Isolation of rat iris pigment epithelial cells

All procedures involving rats adhered to the Association for Research Vision and Ophthalmology (ARVO) Resolution on the Use of Animals in Research, and the guidelines of the UCSF Committee on Animal Research. IPE cells were prepared from 10 to 12 week-old Long Evans rat eyes according to the technique described by Sakuragi *et al.* (Sakuragi *et al.*, 2001). IPE cells were maintained with Ham's F12 (GIBCO BRL, Japan) containing 20% fetal bovine serum (FBS) and the medium was changed every three days. Cells were passaged using 0.125% trypsin containing 0.01% EDTA. We performed three independent experiments for the measurement of phagocytic activities using IPE cells.

Preparation of POS

POS were isolated from adult porcine retinas using sucrose step gradient centrifugation (Papermaster and Dreyer, 1974; Sakuragi *et al.*, 2001). POS suspended in phosphate buffered saline (PBS) were then used for the phagocytosis studies.

Experimental schedules

One day before the addition of POS and BDNF, 2×10^5 IPE cells were plated into each well of a 24-well plate. The sub-confluent IPE cell cultures with or without BDNF were challenged with POS (1×10^7 POS particles/well) diluted with growth medium. LY294002 (Sigma, St. Louis, MO) and PD98059 (Sigma, St. Louis, MO) were added to the medium 30 minutes before the challenge of POS and BDNF. This medium was not exchanged until the end of the evaluation three hours later.

Measurement of phagocytic activity

To determine phagocytic activity three hours after the challenge of POS and BDNF, bound and total POS were differentially stained using a double immunofluorescence staining method (Chaitin and Hall, 1983). Briefly, cells were washed with PBS three times to remove unbound POS and fixed in 3.7% formaldehyde. Bound POS were stained with anti-rhodopsin antiserum (Cosmo Bio Co., Ltd., Tokyo, Japan) using Alexa 594 conjugated antibody as a secondary antibody (Invitrogen, Carlsbad, CA). Cells were opened with 47.5% ethanol, and total POS was stained with anti-rhodopsin antiserum (Cosmo Bio Co., Ltd., Japan) using Alexa 488 conjugated antibody (Invitrogen, Carlsbad, CA). 4,6-Diamidino-2-phenylindole, dihydrochloride (DAPI; Dojindo, Japan) was used for nuclear staining. Each treatment was performed on duplicate wells. Confluent areas of cells were selected, and four separate areas of each well were photographed by using a fluorescent microscope, Axiovert40 (Carl Zeiss, Japan). Fluorescence areas showing bound and total POS were measured by the Zeiss imaging software, AxioVision, and the number of nuclei in the photographed areas was counted.

Statistical analyses

Statistical analysis was performed using GraphPad Prism software (GraphPad Software, San Diego, CA). Bonferroni/Dunn's multiple range test was used for planned comparisons among the various treatment groups. All data obtained from three independent experiments (total of six wells per sample) were used for statistical analysis.

Western blot analysis

Cells were washed with ice-cold PBS three times and the protein was extracted with lysis buffer (10 mM Tris [pH 7.5]; 1% TritonX-100; 0.5% NP-40; 1 mM EDTA; 150 mM NaCl; 1 μg/mL each of aprotin, leupeptin, antipain, and pepstatin A; 1 mM *p*-amidinophenyl methanesulfonyl fluoride; 10 mM *p*-nitrophenyl phosphate; 5 mM sodium pyrophosphate; 0.2 mM sodium molybdate; 10 mM β-glycerophosphate; 50 μM sodium fluoride; 1 mM sodium orthovanadate), put on ice for 30 minutes, and centrifuged at 15,000 rpm at 4°C for 15 minutes. The protein in the supernatant of the lysate was quantified by a use of BCA protein assay kit (Pierce, Rockford, IL). An aliquot of this total protein was mixed with SDS-buffer (50 mM Tris-HCl [pH 6.8]; 2% SDS; 10% glycerol; 6% β-mercaptoethanol), boiled for 5 minutes, and processed for SDS-PAGE.

For Western blots of Akt (Cell Signaling Technology, Beverly, MA), phospho-Akt (Cell Signaling Technology, Beverly, MA), Erk1/2 (BD Bioscience, Franklin Lakes, NJ), and Phospho-Erk1/2 (BD Bioscience, Franklin Lakes, NJ), 10 μg of protein were electrophoresed on 4%–20% Tris-HEPES-SDS-Polyacrylamide gels (Pierce, Rockford, IL) and transferred onto a PVDF membrane. The membranes were bathed with an antibody and then washed three times with TBST [10 mM Tris-HCl (pH 8.0); 150 mM NaCl; 0.1% Tween 20]. Alkaline phosphatase conjugated donkey anti-rabbit IgG (Promega, Madison, WI) or goat anti-mouse IgG (Promega, Madison, WI) was used as a secondary antibody. Protein bands were developed by CDP Star (Amersham Biosciences Corp., Piscataway, NJ) according to the manufacturers instructions.

Results

Measurement of phagocytic activity

To measure the binding and ingestion of POS to IPE cells, we used a double immunofluorescence staining method. As shown in Fig. 1A, the binding of POS to the cell membrane and total POS were visualized as red and green fluorescence, respectively, by differentially staining with anti-

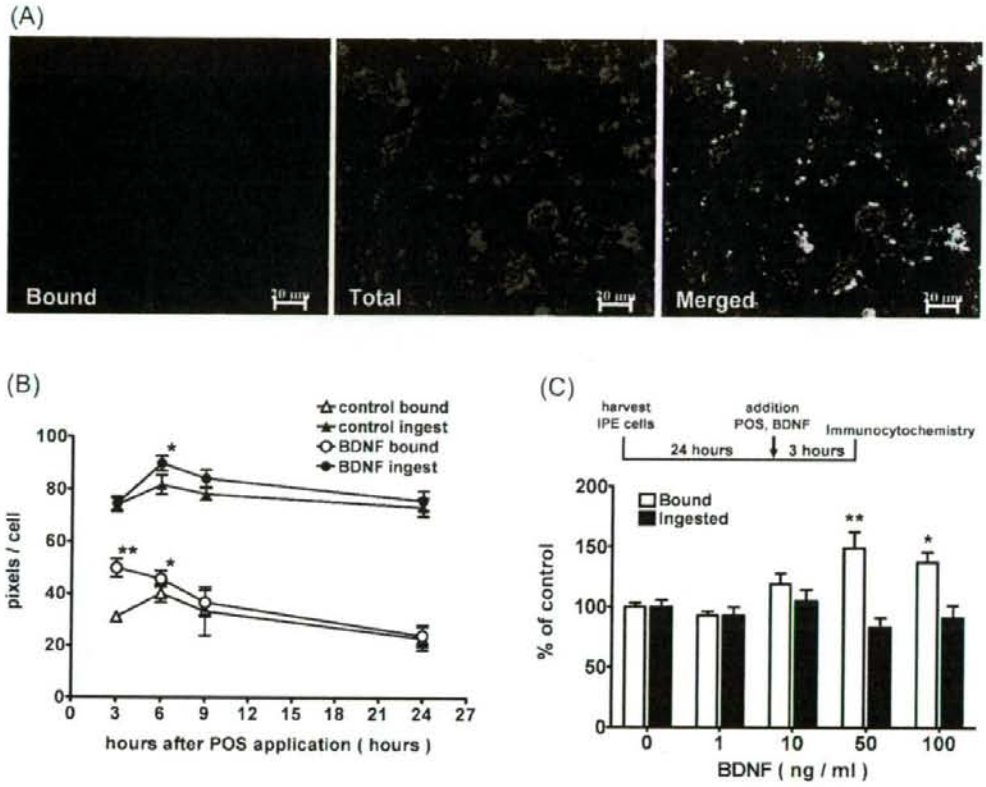

Fig. 1. Phagocytic activities of IPE cells cultured in the medium with or without BDNF. Fluorescent microphotographs of POS phagocytosed-IPE cells cultured in the growth medium without BDNF three hours after the POS-application (A). Changes of phagocytic activities after the POS application. BDNF (50 ng/ml) was added to the growth medium at the same time as the POS application. Phagocytic activity was calculated as fluorescence area per cell (B). IPE cells were cultured in the medium containing various concentrations of BDNF and purified porcine POS for three hours (C). Phagocytic activities were represented as a percent of the control. Statistical analysis was performed by the unpaired t-test (*,**$p<0.05$, 0.01).

rhodopsin antibody. Both phagocytic activities of binding and ingestion in IPE cells cultured with normal medium, gradually increased up to 6 hours after the POS application. When BDNF was added at the same time with the POS application, the POS binding activity was markedly increased at 3 hours after the application (Fig. 1B). The binding activity by the addition of BDNF showed a dose-dependent increase. At the concentration of 50 ng/ml, the binding of POS increased up to 150% compared to the control (Fig. 1C). Ingestion of POS, however, was not affected throughout the concentrations used in this study. To investigate the signal transduction pathways of BDNF, a phosphatidylinositol 3-kinase (PI3K) inhibitor, LY294002, and MAPK/ERK kinase (MEK) inhibitor, PD98059, were used for this study. LY294002 had no effect on the binding and ingestion of POS in BDNF-treated IPE cells (Fig. 2A). On the other hand, PD98059 completely inhibited the increase of POS binding in BDNF-treated cells and also decreased the ingestion of POS in BDNF-treated IPE cells and control IPE cells (Fig. 2B, C). PD98059 did not significantly decrease the binding of POS in control IPE cells (Fig. 2C).

Western blots showed no change of Akt phosphorylation by the addition of POS (Fig. 3A). In contrast, the phosphorylation of ERK1/2 was induced by the addition of POS (Fig. 3B). BDNF induced the phosphorylation both of Akt and ERK1/2 (Fig. 3A, B right lane). Specifically, the ERK was markedly phosphorylated by the addition of BDNF (Fig. 3B right lane). Its phosphorylation was inhibited by the addition of each inhibitor (Fig. 3C, D).